

Twist-programmable superconductivity in spin-orbit-coupled bilayer graphene

<https://doi.org/10.1038/s41586-025-08959-3>

Received: 5 August 2024

Accepted: 1 April 2025

Published online: 07 May 2025

 Check for updates

Yiran Zhang^{1,2,3✉}, Gal Shavit^{2,3,4}, Huiyang Ma^{5,6}, Youngjoon Han^{2,3}, Chi Wang Siu^{1,2}, Ankan Mukherjee^{1,2}, Kenji Watanabe⁷, Takashi Taniguchi⁷, David Hsieh^{2,3}, Cyprian Lewandowski^{5,6}, Felix von Oppen⁸, Yuval Oreg⁹ & Stevan Nadj-Perge^{1,2✉}

The relative twist angle between layers of near-lattice-matched van der Waals materials is critical for the emergent phenomena associated with moiré flat bands^{1–3}. However, the concept of angle rotation control is not exclusive to moiré superlattices in which electrons directly experience a twist-angle-dependent periodic potential. Instead, it can also be used to induce programmable symmetry-breaking perturbations with the goal of stabilizing desired correlated states. Here we experimentally demonstrate ‘moiréless’ twist-tuning of superconductivity together with other correlated orders in Bernal bilayer graphene proximitized by tungsten diselenide. The precise alignment between the two materials systematically controls the strength of induced Ising spin-orbit coupling (SOC), profoundly altering the phase diagram. As Ising SOC is increased, superconductivity onsets at a higher displacement field and features a higher critical temperature, reaching up to 0.5 K. Within the main superconducting dome and in the strong Ising SOC limit, we find an unusual phase transition characterized by a nematic redistribution of holes among trigonally warped Fermi pockets and enhanced resilience to in-plane magnetic fields. The superconducting behaviour is theoretically compatible with the prominent role of interband interactions between symmetry-breaking Fermi pockets. Moreover, we identify two additional superconducting regions, one of which descends from an inter-valley coherent normal state and shows a Pauli-limit violation ratio exceeding 40, among the highest for all known superconductors^{4–7}. Our results provide insights into ultraclean graphene superconductors and underscore the potential of utilizing moiréless-twist engineering across a wide range of van der Waals heterostructures.

In a large electrical displacement field, the electronic bands of Bernal bilayer graphene (BLG) flatten out around the corners of the Brillouin zone, giving rise to various correlated phases that spontaneously break BLG symmetries^{4,8,9}. These correlated phases naturally compete with each other and, therefore, are highly sensitive to explicit symmetry-breaking perturbations. One way to induce such perturbations is by placing BLG adjacent to transition-metal dichalcogenides such as tungsten diselenide (WSe₂). The spin-orbit coupling (SOC) perturbations induced by WSe₂ (refs. 10–16) alter the phase diagram, remarkably enabling the superconductivity in BLG⁴ to appear at zero magnetic field and boosting the critical temperature significantly^{17–19}. However, the nature and the extent of this enhancement, and more generally, the impact of SOC on the correlated phases of BLG and related graphene systems, remain elusive.

Programmable Ising SOC

Theoretically, the induced SOC is predicted to depend on the relative twist angle θ between WSe₂ and graphene^{16,20–23} (Fig. 1a).

This dependence, however, has not been experimentally studied or utilized with systematic control. Here we use this tuning knob to explore how Ising SOC modifies the correlated phases and emerging superconductivity in BLG. This approach offers several unique opportunities: (1) the strength of the induced Ising SOC in BLG can be precisely quantified; (2) the induced SOC is much less sensitive to twist-angle variations, allowing for fine control; and (3) the proximity to WSe₂ does not induce additional disorder, promoting reproducibility. We investigated a series of BLG–WSe₂ devices (Fig. 1b) fabricated from the same BLG and WSe₂ crystals, separating the large BLG flake into multiple pieces²⁴. With the first BLG piece roughly lattice-aligned with WSe₂ ($\theta \approx 0^\circ$), the following ones were sequentially twisted relative to WSe₂ with an approximately 6° increment (see Methods and Extended Data Fig. 1 for device fabrication).

To characterize the SOC in our devices, we first perform high-resolution measurements of Shubnikov–de Haas oscillations (Fig. 1f,g) in regions of the n – D phase diagram (n is the doping density, and D is the electrical displacement field) that are well described by

¹T. J. Watson Laboratory of Applied Physics, California Institute of Technology, Pasadena, CA, USA. ²Institute for Quantum Information and Matter, California Institute of Technology, Pasadena, CA, USA. ³Department of Physics, California Institute of Technology, Pasadena, CA, USA. ⁴Walter Burke Institute of Theoretical Physics, California Institute of Technology, Pasadena, CA, USA.

⁵National High Magnetic Field Laboratory, Tallahassee, FL, USA. ⁶Department of Physics, Florida State University, Tallahassee, FL, USA. ⁷National Institute for Materials Science, Tsukuba, Japan.

⁸Dahlem Center for Complex Quantum Systems and Fachbereich Physik, Freie Universität Berlin, Berlin, Germany. ⁹Department of Condensed Matter Physics, Weizmann Institute of Science, Rehovot, Israel. [✉]e-mail: yzhang7@caltech.edu; s.nadj-perge@caltech.edu

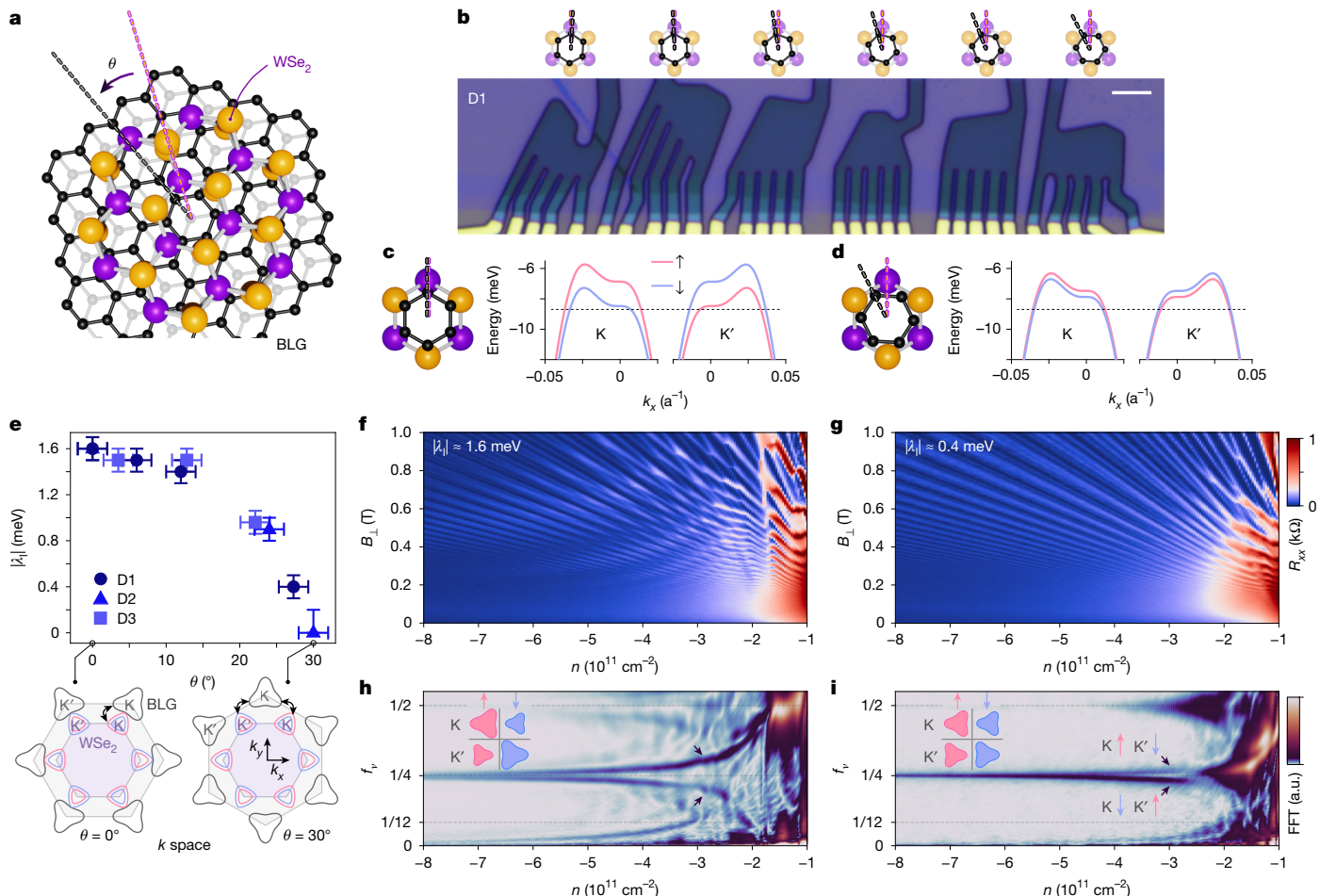


Fig. 1 | Programmable Ising SOC by interfacial twisting between BLG and WSe₂.

a, Schematic showing the twisting of the BLG–WSe₂ interface. **b**, Optical image of the device set D1. Crystal axes of graphene and WSe₂ are rotated relative to each other with angles θ of approximately 0°, 6°, 12°, 18°, 24° and 30° for the 6 devices, respectively. Scale bar, 5 μm . **c,d**, Non-interacting valence bands of BLG near the K and K' points of the Brillouin zone at $D/\epsilon_0 = 0.2 \text{ V nm}^{-1}$, with proximitized Ising SOC $|\lambda_i| \approx 1.6 \text{ meV}$ (**c**) and $|\lambda_i| \approx 0.4 \text{ meV}$ (**d**). Here k is the momentum, and $a = 0.246 \text{ nm}$ is the graphene lattice constant. The dashed horizontal lines correspond to the Fermi level; the up and down arrows

represent spins. **e**, Ising SOC strength $|\lambda_i|$ versus BLG–WSe₂ interfacial twist angle θ ; data were extracted from three sets of devices D1–D3. The bottom schematics show the relative rotation between the BLG and WSe₂ Brillouin zones. **f,g**, R_{xx} versus B_\perp and doping n measured at $D/\epsilon_0 = 0.2 \text{ V nm}^{-1}$ for devices with $|\lambda_i| \approx 1.6 \text{ meV}$ (**f**) and $|\lambda_i| \approx 0.4 \text{ meV}$ (**g**). **h,i**, Fast Fourier transform (FFT) of $R_{xx}(1/B_\perp)$ (using data within $0.05 < B_\perp < 0.8 \text{ T}$) versus n and f_v . The arrowed FFT splittings reflect the Ising-induced Fermi-surface imbalance, where larger Ising SOC (**h**) features a larger splitting than small Ising SOC (**i**).

non-interacting theory (Supplementary Information section 1). When a positive D field $D/\epsilon_0 = 0.2 \text{ V nm}^{-1}$ is applied, the hole-carrier wavefunctions are strongly polarized towards the top graphene layer adjacent to WSe₂, which in turn induces Ising SOC in BLG^{14,17–19,25,26} (see Methods and Extended Data Fig. 2 for further discussion). In this regime, we observe a clear beating pattern in longitudinal resistance R_{xx} as a function of out-of-plane magnetic field (B_\perp) at higher doping densities (Fig. 1f), indicating two close oscillation frequencies originating from Fermi pockets of slightly different sizes. The Fermi-surface imbalance is revealed by normalizing the oscillation frequencies of $R_{xx}(1/B_\perp)$ to the Luttinger volume corresponding to the total doping density. The resulting normalized frequency f_v reveals the fraction of the total Fermi surface area enclosed by a cyclotron orbit. Figure 1h,i shows a comparison of the density-dependent frequencies f_v from two devices with twist angles $\theta \approx 0^\circ$ and $\theta \approx 30^\circ$, respectively. In both cases, two frequencies, $f_v^{(1)}$ and $f_v^{(2)}$, are found satisfying $f_v^{(1)} + f_v^{(2)} = 1/2$. These frequencies can be understood as a splitting from $f_v = 1/4$, which signals the broken four-fold spin–valley symmetry (Fig. 1c,d): Ising SOC separates two pairs of spin–valley-locked bands with slightly different Fermi-surface areas (schematics in Fig. 1h,i).

The induced Ising SOC is modulated by the twist angle θ between WSe₂ and BLG. This is evident from the more pronounced splitting shown in Fig. 1h compared with the one in Fig. 1i. By extracting the sizes of the Fermi pockets corresponding to spin–valley-locked bands (Methods and Extended Data Fig. 2) and comparing them with band-structure calculations, we precisely quantify the Ising SOC strength, $|\lambda_i| \approx 1.6 \text{ meV}$ and $|\lambda_i| \approx 0.4 \text{ meV}$ in Fig. 1h,i, respectively. Figure 1e summarizes systematic measurements across three sets of moiréless twisting BLG–WSe₂ devices (D1–D3; Methods and Supplementary Figs. 1–3), all of which show robust θ -modulated Ising SOC strengths. Our results are consistent with the picture that virtual interlayer tunnelling is responsible for the induced SOC. When the lattices of BLG and WSe₂ are angle-aligned, that is, $\theta \approx 0^\circ$, the K and K' valleys of BLG couple more effectively to one of the two valleys of WSe₂ (left schematic in Fig. 1e), resulting in a large induced Ising SOC. In contrast, for $\theta \approx 30^\circ$, the inter-valley and intra-valley tunnelling between WSe₂ and BLG have the same amplitude owing to reflection symmetry (right schematic in Fig. 1e). The induced Ising SOC in BLG vanishes accordingly²⁷. The overall θ dependence and the magnitude of Ising SOC are qualitatively consistent with predictions^{16,20–23}.

Twist-programmable superconductivity

Using the exquisite twist-angle control of the Ising SOC strength, we explore the SOC-dependent correlated phase diagrams at large D fields. Devices with various Ising strengths all show characteristic R_{xx} features that are associated with strong correlations and superconductivity stabilized at zero magnetic field^{17–19} (Fig. 2a–d; see Extended Data Fig. 3 for all the n - D phase diagrams). Importantly, the main superconducting pocket, which emerges from a polarized state with a dominant population of two out of the four spin–valley flavours^{17,18}, shows a strong dependence on the strength of Ising SOC. For low Ising SOC ($|\lambda_l| \approx 0.4$ meV; Fig. 2a), the superconducting region occupies a large D -field range, starting from $D/\epsilon_0 \approx 0.3$ V nm^{−1} and extending up to $D/\epsilon_0 \approx 1.25$ V nm^{−1}. For large Ising SOC ($|\lambda_l| \approx 1.5$ meV; Fig. 2d), however, superconductivity onsets only at $D/\epsilon_0 \approx 0.9$ V nm^{−1}. Overall, the value D_{onset} marking the onset of the superconducting pocket grows with increasing $|\lambda_l|$ (Fig. 2e).

The observed trend of D_{onset} can be understood in a simple model invoking the interband interactions between the majority ($K\uparrow, K'\downarrow$) and the minority ($K\downarrow, K'\uparrow$) spin–valley flavours (Fig. 2g,h). Irrespective of the pairing mechanism, superconductivity requires an attractive interaction to overcome the renormalized Coulomb repulsion^{28,29}, commonly quantified by Tolmachev–Anderson–Morel pseudopotential^{30,31} μ^* . When μ^* is large, electrons do not form pairs and superconductivity vanishes. The generalized multiband value, which takes into account majority and minority spin–valley flavours, μ_{multi}^* (Methods and Supplementary Information sections 2–4) is plotted in Fig. 2h for two values of Ising SOC. Remarkably, μ_{multi}^* grows with increasing $|\lambda_l|$ and decreases at higher D fields. Thus, the threshold for superconductivity, as implied by a sufficiently weak μ_{multi}^* , aligns with the experimental D_{onset} trend. The connection between μ_{multi}^* and Ising SOC arises owing to interband interactions. These interactions allow scattering of pairs between majority and minority bands (Fig. 2g), greatly enhancing screening of the bare repulsion compared with the band-decoupled case. A larger density imbalance between the bands, as dictated by stronger Ising SOC, shrinks the phase space where both bands have a large density of states (DOS) near the Fermi level (right schematic in Fig. 2h). Consequently, the interband interactions are suppressed, μ_{multi}^* grows and superconductivity diminishes.

Intriguingly, the superconducting critical temperature T_c also shows a striking dependence on $|\lambda_l|$. Whereas D_{onset} is smaller and superconductivity persists over a wide range of D fields for small Ising SOC, the critical temperature remains low throughout and saturates at $T_c \approx 150$ mK (Fig. 2i,j). In contrast, for large Ising SOC, superconductivity onsets only at higher D fields, but T_c quickly increases, reaching $T_c \approx 500$ mK at the optimal D (Fig. 2l,m). This is the highest T_c reported for crystalline (untwisted) graphene systems. Thus, the optimal critical temperature also shows an increasing trend with $|\lambda_l|$ (Fig. 2f; see Supplementary Fig. 4 for $|\lambda_l| \approx 0$ meV). A detailed three-dimensional map of the optimal critical temperature T_c^{optimal} versus D field and $|\lambda_l|$ is plotted in Fig. 2k. These observations motivate further investigations of BLG with even stronger Ising SOC^{32,33}.

Three superconducting regions

Devices with large Ising SOC further reveal two additional superconducting pockets (1.4 meV $\lesssim |\lambda_l| \lesssim 1.6$ meV; Figs. 2c,d and 3a, and Extended Data Fig. 3). We refer to the observed superconducting regions as SC_1 , SC_2 and SC_3 , enumerated from higher to lower hole doping, respectively (with the main superconducting region being SC_2 ; see Extended Data Fig. 4 and Supplementary Information section 6 for additional characterizations and discussion). Each superconducting pocket descends from a distinct flavour-symmetry-breaking normal state (Fig. 3b–f) and is terminated by a first-order phase transition (marked by black dashed lines) on the low-doping side. Regions SC_1 ,

SC_2 and SC_3 feature optimal critical temperatures $T_c \approx 60$ mK, $T_c \approx 500$ mK and $T_c \approx 100$ mK, respectively (Fig. 3b,d, insets). The normal state of SC_1 can be directly related to the non-interacting band structure. Quantum oscillations in this regime ($-9 \times 10^{11} \lesssim n \lesssim -7.6 \times 10^{11}$ cm^{−2}; Fig. 3c) show 2 main frequencies (marked by blue and orange arrows) obeying $2f_v^{(1)} + 6f_v^{(2)} \approx 1$. This indicates two Ising-majority Fermi pockets and six Ising-minority trigonal-warping pockets^{18,34} (Fig. 3c, left schematic); we denote the flavour-polarized phase as FP(2, 6) (FP(n, m) denotes a flavour-polarized phase with n and m degenerate-sized Fermi pockets, from large to small).

Ultrahigh-resolution quantum oscillations reveal the unusual Fermi surfaces in the correlated normal states forming SC_2 and SC_3 . At higher doping of SC_2 ($n \lesssim -8.25 \times 10^{11}$ cm^{−2}; Fig. 3e), 2 dominant oscillation frequencies, marked by blue ($f_v^{(1)}$) and orange ($f_v^{(2)}$) lines in Fig. 3f, satisfy $2f_v^{(1)} + 4f_v^{(2)} \approx 1$ (black line). Thus, the flavour-polarized phase hosts two majority and four minority Fermi pockets, denoted as FP(2, 4). The occupation of two out of the three trigonal-warping pockets for each minority flavour implies a nematic normal state that breaks the C_3 rotational symmetry¹⁸ (Fig. 3f, left schematic). Remarkably, we observe a different Fermi-pocket configuration within the same superconducting pocket at $-8.25 \times 10^{11} \lesssim n \lesssim -7.1 \times 10^{11}$ cm^{−2}. The lowest third frequency $f_v^{(3)}$ is clearly resolved (green line in Fig. 3f; Methods and Extended Data Figs. 5–7). The value of $f_v^{(3)}$ rapidly decreases to zero at the low-doping phase boundary, implying that two out of the four minority Fermi pockets shrink considerably in this density range. We denote this phase as FP(2, 2, 2) given the relation $2f_v^{(1)} + 2f_v^{(2)} + 2f_v^{(3)} \approx 1$. Here, the second and the third ‘2’ imply an additional broken symmetry within the trigonal-warping pockets^{35,36} (orange and green pockets of the middle schematic in Fig. 3f), signalling a nematic redistribution of holes. This continuous transition from FP(2, 2, 2) to FP(2, 4) has a remarkable impact on the in-plane magnetic-field response of SC_2 (Fig. 4).

An exceptional correlated phase denoted FP(1, 3, 1) emerges upon further decreasing the doping ($-7.1 \times 10^{11} \lesssim n \lesssim -5.7 \times 10^{11}$ cm^{−2}; Fig. 3e,f). The three Fermi-surface frequencies obey $f_v^{(4)} + 3f_v^{(5)} + f_v^{(6)} \approx 1$, with $f_v^{(4)}$ being larger than 1/2, ensuring that the largest Fermi pocket is non-degenerate (Methods and Extended Data Figs. 8–10). Remarkably, this normal state supports SC_3 , although all Fermi pockets have odd multiplicities. The combination of superconductivity and odd multiplicities strongly points at an inter-valley coherent state^{37–43} (purple schematic in Fig. 3f). This is further corroborated by the B_{\perp} -field response of the phase boundaries³⁹ (Methods and Extended Data Fig. 11). The odd multiplicity of all Fermi pockets excludes the possibility of conventional s-wave pairing, suggesting unconventional superconductivity. Moreover, provided that the pockets are intrinsically superconducting, the number of three mid-size Fermi pockets ($f_v^{(5)}$) implies time-reversal symmetry breaking regardless of the inter-valley coherent nature^{41,44–46}. Alternative exotic scenarios are not precluded, for example, the valleys of FP(1, 3, 1) could still enjoy independence, in which case, the resulting superconductivity would strongly break time-reversal symmetry, promoting chiral finite-momentum pairing.

Ultrastrong magnetic-field resilience

All three superconducting pockets show extraordinary resilience to in-plane magnetic field B_{\parallel} . SC_1 has a critical field $B_{\text{c1}} \approx 2.5$ T, substantially higher than observed previously¹⁸ (Supplementary Fig. 5). SC_2 and SC_3 show distinct B_{\parallel} response, reflecting the highly unusual intertwining with the underlying normal states. Figure 4a,b shows the dependence of R_{xx} on B_{\parallel} (Fig. 4a) and temperature (Fig. 4b). SC_2 occupies a significantly larger doping range, and its optimal T_c is roughly five times that of SC_3 . In comparison, the two superconducting regions show a striking response to B_{\parallel} . Whereas SC_2 is fully suppressed by $B_{\parallel} \approx 3$ T, SC_3 persists up to $B_{\parallel} = 7$ T at the phase boundary. Crucially, the T_c^{optimal} of SC_3 appears to be insensitive to B_{\parallel} (Fig. 4e and Supplementary Fig. 6),

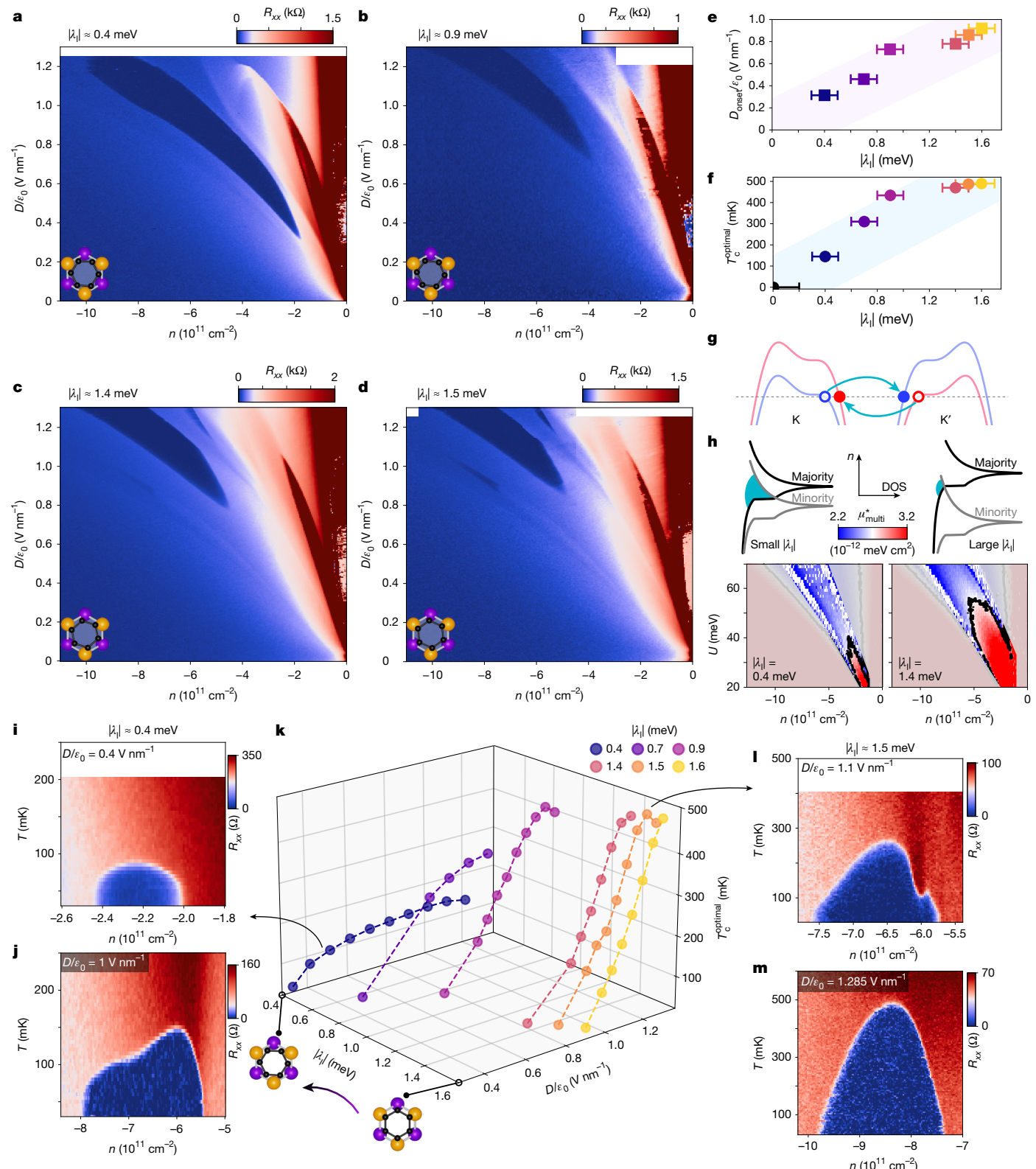


Fig. 2 | Twist-programmable superconducting phase diagram. **a-d**, R_{xx} versus n and D for devices with $|\lambda_i| \approx 0.4$ meV (a), $|\lambda_i| \approx 0.9$ meV (b), $|\lambda_i| \approx 1.4$ meV (c) and $|\lambda_i| \approx 1.5$ meV (d). **e,f**, Displacement field at which superconductivity onsets D_{onset} (e) and optimal critical temperature T_c^{optimal} (f) versus $|\lambda_i|$. The black dot in f represents the case at $|\lambda_i| \approx 0$ meV; see also Methods and Supplementary Fig. 4. The error bars come from uncertainty in extraction of the Ising SOC strength (see Methods and Extended Data Fig. 2). The different colours represent different $|\lambda_i|$; shaded areas indicate increasing D_{onset} and T_c^{optimal} with $|\lambda_i|$. **g**, Schematic showing the interband interactions (turquoise arrows)

between majority (filled dots) and minority (open dots) hole flavours. Pink and blue lines indicate spin-up and spin-down valence bands, respectively. **h**, Bottom: μ_{multi}^* versus n and interlayer potential difference U for $|\lambda_i| = 0.4$ meV (left) and $|\lambda_i| = 1.4$ meV (right). Top: schematics showing the Ising-imbalanced DOS; turquoise regions indicate where both bands have large DOS. **i,j**, R_{xx} versus n and temperature for a device with $|\lambda_i| \approx 0.4$ meV, measured at $D/\varepsilon_0 = 0.4$ V nm $^{-1}$ (i) and $D/\varepsilon_0 = 1$ V nm $^{-1}$ (j). **k**, Optimal critical temperature T_c^{optimal} versus $|\lambda_i|$ and D . **l,m**, R_{xx} versus n and temperature for a device with $|\lambda_i| \approx 1.5$ meV, measured at $D/\varepsilon_0 = 1.1$ V nm $^{-1}$ (l) and $D/\varepsilon_0 = 1.285$ V nm $^{-1}$ (m).

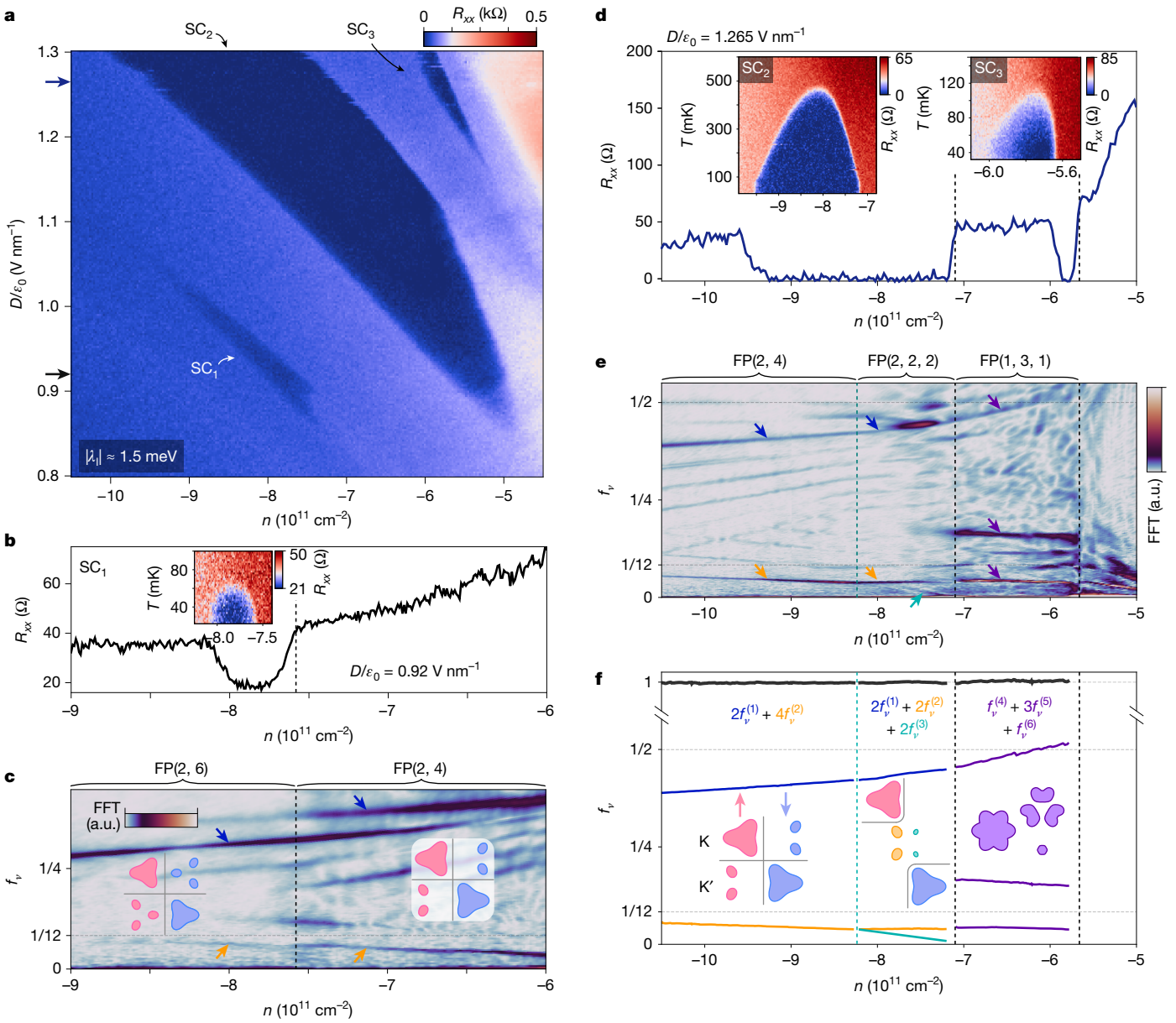


Fig. 3 | Superconductivity across nematic redistribution and from inter-valley coherence. **a**, R_{xx} versus n and D for a device with Ising SOC strength $|\lambda_I| \approx 1.5$ meV, focusing around the phase space where the three superconducting regions coexist. The black and blue arrows on the left mark the D fields at which the data in **b** and **d** are measured, respectively. **b**, R_{xx} versus n measured at $D/\epsilon_0 = 0.92$ V nm $^{-1}$. Inset: R_{xx} versus n and temperature for the superconducting dome SC₁. **c**, Frequency-normalized FFT of $R_{xx}(1/B_\perp)$ (using data within $0.08 < B_\perp < 0.4$ T) over the same doping range as in **b**; schematics show the corresponding flavour-symmetry-breaking Fermi surfaces. The arrows mark the primary FFT peaks. **d**, R_{xx} versus n measured at $D/\epsilon_0 = 1.265$ V nm $^{-1}$.

with the superconducting domes at $B_\parallel = 0$ T and $B_\parallel = 3$ T being almost the same (Fig. 4c,d). The Pauli limit B_p is related to the zero-magnetic-field critical temperature $T_c(0)$ as $B_p = 1.86$ T K $^{-1} \times T_c(0)$. $T_c(0) = 100$ mK for SC₃ would produce $B_p = 0.186$ T. Thus, the observed $B_{\text{cl}} = 7$ T yields a Pauli-limit violation ratio (PVR) $B_{\text{cl}}/B_p \approx 40$, placing SC₃ among the superconducting phases with the highest PVR $^{4-7}$. It is noted that the exceedingly large PVR presents only in SC₃ with odd Fermi-pocket multiplicities, further reflecting its remarkable nature.

Although SC₂ has a significantly lower PVR, it features two doping regions with distinct B_\parallel responses (Fig. 4f,g) that are directly intertwined with the continuous transition from FP(2, 2, 2) to FP(2, 4) (Fig. 4h,i).

Insets: R_{xx} versus n and temperature for the superconducting domes SC₂ (left) and SC₃ (right). **e**, Frequency-normalized FFT of $R_{xx}(1/B_\perp)$ (using data within $0.05 < B_\perp < 0.8$ T to resolve $f_v^{(3)}$) over the same doping range as in **d**. The arrows mark the primary FFT peaks, as shown in **f**. The green dashed line marks the transition from FP(2, 2, 2) to FP(2, 4); the black dashed lines mark first-order symmetry-breaking transitions. **f**, Intensity peaks in f_v extracted from **e**. The black solid lines around $f_v = 1$ indicate the results from the Luttinger sum rule. Schematics from left to right correspond to nematic FP(2, 4), nematic FP(2, 2, 2), and inter-valley coherent FP(1, 3, 1).

Figure 4f,g shows representative R_{xx} versus temperature and B_\parallel measured in the overdoped and underdoped regions ($n = -8.5 \times 10^{11}$ cm $^{-2}$ and $n = -6.9 \times 10^{11}$ cm $^{-2}$, respectively) for $D/\epsilon_0 = 1.2$ V nm $^{-2}$. SC₂ shows the same $T_c(0) \approx 200$ mK at both doping densities, but the B_\parallel responses are distinct. The overdoped T_c is quickly suppressed by B_\parallel following a conventional quadratic scaling (Fig. 4f). The underdoped T_c , however, is insensitive to B_\parallel for $B_\parallel \leq 1$ T (Fig. 4g), with the depairing at $B_\parallel > 1.5$ T probably owing to the Fermi-surface changes induced by B_\parallel .

We fit T_c versus B_\parallel by $T_c(B_\parallel) = T_c(0) - \alpha B_\parallel^2$, where α quantifies the pair-breaking tendency of B_\parallel . The resulting α shows a striking dependence on doping (Fig. 4h). At higher doping, α plateaus around 0.08 K T $^{-2}$;

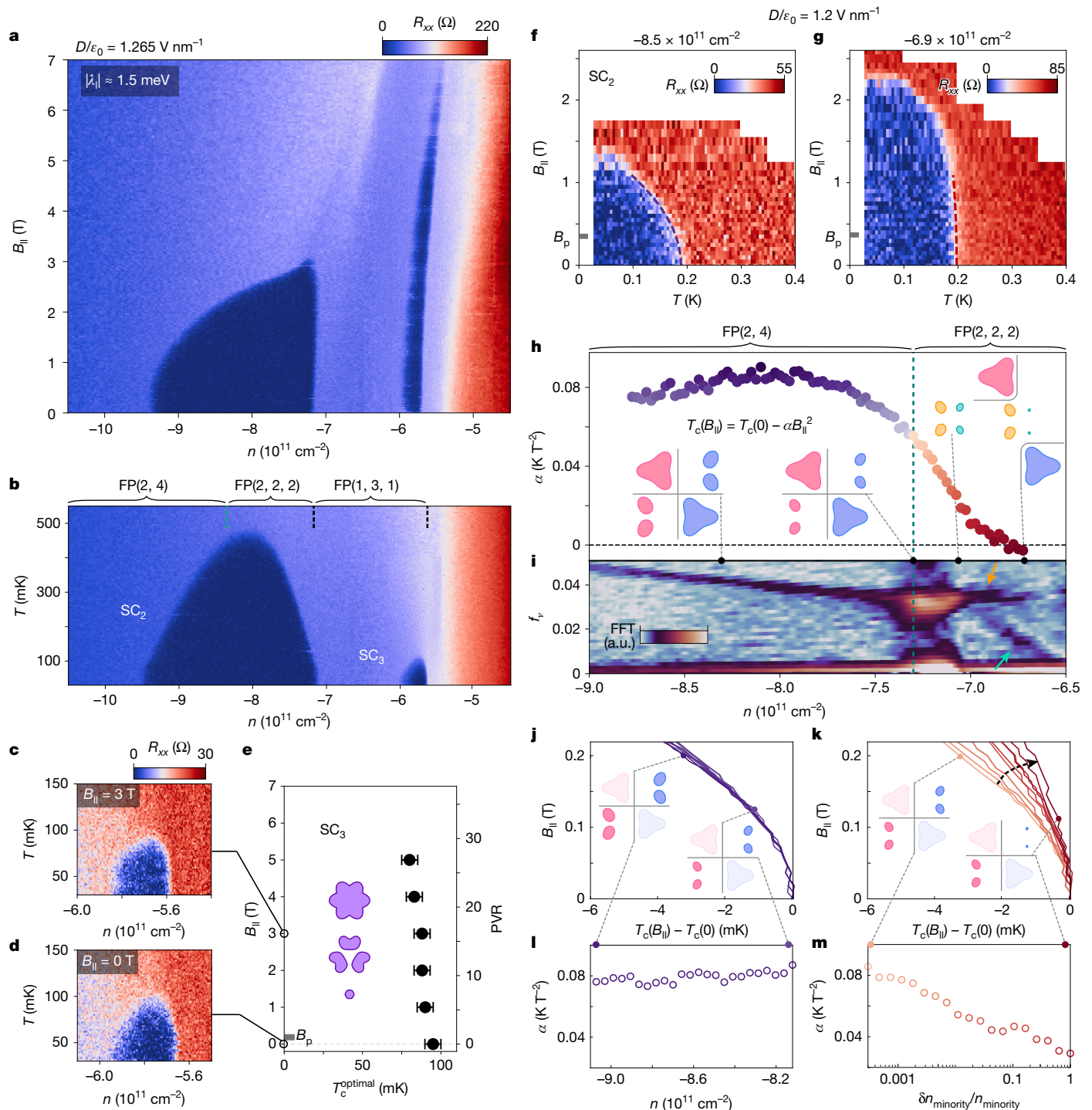


Fig. 4 | Ultrahigh Pauli-limit violation and nematicity-intertwined B_{\parallel} depairing. **a**, R_{xx} versus n and B_{\parallel} at $D/\epsilon_0 = 1.265 \text{ V nm}^{-1}$ for a device with $|\lambda_i| \approx 1.5 \text{ meV}$. **b**, R_{xx} versus n and temperature at the same D . The green dashed line marks the density where nematic redistribution occurs. The black dashed lines mark first-order symmetry-breaking transitions. **c,d**, R_{xx} versus n and temperature for SC₃ measured at $B_{\parallel} = 0 \text{ T}$ (**c**) and $B_{\parallel} = 3 \text{ T}$ (**d**). **e**, T_c^{optimal} of SC₃ versus B_{\parallel} . The grey bar marks the Pauli limit. The error bars are determined by the temperature at which R_{xx} corresponds to 10% and 90% of the normal-state resistance. The purple schematic shows the FP(1, 3, 1) Fermi surfaces. **f,g**, R_{xx}

versus temperature and B_{\parallel} at $n = -8.5 \times 10^{11} \text{ cm}^{-2}$ (**f**) and $n = -6.9 \times 10^{11} \text{ cm}^{-2}$ (**g**) for $D/\epsilon_0 = 1.2 \text{ V nm}^{-1}$. The coloured dashed lines are quadratic fitting. **h**, α versus n within the SC₂ at $D/\epsilon_0 = 1.2 \text{ V nm}^{-1}$. **i**, Normalized FFT of $R_{xx}(1/B_{\perp})$ (using data within $0.05 < B_{\perp} < 0.8 \text{ T}$ to resolve $f_y^{(3)}$) over the same n and D range as in **h**, focusing at low frequencies. The green dashed line marks the nematic redistribution of holes from FP(2, 4) to FP(2, 2, 2). Schematics in **h** show the Fermi-surface evolution versus n . **j,k**, Theoretical B_{\parallel} depairing with the prominent interband pairing (**j**) and the suppressed case by valley polarization (**k**). **l,m**, Theoretical α versus n for FP(2, 4) (**l**) and versus minority imbalance $\delta n_{\text{minority}}/n_{\text{minority}}$ for FP(2, 2, 2) (**m**).

at lower doping, α approaches zero, indicating vanishing sensitivity to B_{\parallel} . Importantly, the qualitative change in α (Fig. 4h) coincides with the redistribution of the trigonal-warping pockets (Fig. 4i). The region with the plateau ($-8.8 \times 10^{11} \lesssim n \lesssim -7.3 \times 10^{11} \text{ cm}^{-2}$) and the region

with the rapidly changing α ($-7.3 \times 10^{11} \lesssim n \lesssim -6.6 \times 10^{11} \text{ cm}^{-2}$) correspond to the FP(2, 4) and FP(2, 2, 2) phases, respectively. Within the FP(2, 2, 2), both the value of α and the size of the smallest Fermi pockets (green pockets in Fig. 4h) approach zero at the phase boundary

($n \approx -6.6 \times 10^{11} \text{ cm}^{-2}$). These observations suggest that the smallest Fermi pockets determine the B_{\parallel} response (see also Supplementary Figs. 7–9).

The disparity in the B_{\parallel} response of the two SC_2 regions may also be attributed to the prominence of majority–minority interband interactions, so that the B_{\parallel} response (Fig. 4f–i) and the observed D_{onset} trend (Fig. 2e) share a common microscopic origin (Supplementary Information section 7). The magnetic field causes majority-band (minority-band) spins to cant towards (away from) the magnetic-field direction^{41,47}. As a consequence, Cooper pair scattering between the bands is suppressed, and the applied B_{\parallel} leads to an appreciable decrease in T_c (Fig. 4j,l). Conversely, if minority bands become valley-polarized (consistent with FP(2, 2, 2), right schematic in Fig. 4k), one expects the adverse magnetic-field effects on the interband interaction to gradually disappear, making the superconductor less field-sensitive (Fig. 4k,m). This coincides with the experimental trend in Fig. 4f–i. The above mechanism is consistent with the PVR hierarchy of SC_1 , SC_2 and SC_3 (Supplementary Information section 7). The conventional depairing mechanisms within the Ising superconductor framework^{17,48–50}, however, are qualitatively inconsistent with our observations (Methods and Supplementary Information section 8).

Unprecedented control over the strength of Ising SOC in BLG allowed us to explore its rich set of superconducting regions systematically. Superconductivity occurs for a diverse set of Fermi-pocket configurations, including for Fermi pockets with odd multiplicity pointing at unconventional superconductivity. Remarkably, all the superconductors show distinctive resilience to an in-plane magnetic field. A newly discovered inter-valley coherent configuration shows one of the highest PVR values for any superconductor so far. More generally, the approach of inducing tunable symmetry-breaking fields via moiré-less twisting can be applied to a broad family of van der Waals materials and extended beyond SOC to include magnetism, charge orders and so on. This opens promising avenues towards tailoring exotic phases of matter on demand.

Online content

Any methods, additional references, Nature Portfolio reporting summaries, source data, extended data, supplementary information, acknowledgements, peer review information; details of author contributions and competing interests; and statements of data and code availability are available at <https://doi.org/10.1038/s41586-025-08959-3>.

1. Bistritzer, R. & MacDonald, A. H. Moiré bands in twisted double-layer graphene. *Proc. Natl Acad. Sci. USA* **108**, 12233–12237 (2011).
2. Cao, Y. et al. Correlated insulator behaviour at half-filling in magic-angle graphene superlattices. *Nature* **556**, 80–84 (2018).
3. Cao, Y. et al. Unconventional superconductivity in magic-angle graphene superlattices. *Nature* **556**, 43–50 (2018).
4. Zhou, H. et al. Isospin magnetism and spin-polarized superconductivity in Bernal bilayer graphene. *Science* **375**, 774–778 (2022).
5. Ran, S. et al. Extreme magnetic field-boosted superconductivity. *Nat. Phys.* **15**, 1250–1254 (2019).
6. Ran, S. et al. Nearly ferromagnetic spin-triplet superconductivity. *Science* **365**, 684–687 (2019).
7. Lu, J. et al. Full superconducting dome of strong Ising protection in gated monolayer WS_2 . *Proc. Natl Acad. Sci. USA* **115**, 3551–3556 (2018).
8. de la Barrera, S. C. et al. Cascade of isospin phase transitions in Bernal-stacked bilayer graphene at zero magnetic field. *Nat. Phys.* **18**, 771–775 (2022).
9. Seiler, A. M. et al. Quantum cascade of correlated phases in trigonally warped bilayer graphene. *Nature* **608**, 298–302 (2022).
10. Wang, Z. et al. Origin and magnitude of ‘designer’ spin-orbit interaction in graphene on semiconducting transition metal dichalcogenides. *Phys. Rev. X* **6**, 041020 (2016).
11. Gmitra, M. & Fabian, J. Proximity effects in bilayer graphene on monolayer WSe_2 : field-effect spin valley locking, spin-orbit valve, and spin transistor. *Phys. Rev. Lett.* **119**, 146401 (2017).
12. Khoo, J. Y., Morpurgo, A. F. & Levitov, L. On-demand spin-orbit interaction from which-layer tunability in bilayer graphene. *Nano Lett.* **17**, 7003–7008 (2017).
13. Khoo, J. Y. & Levitov, L. Tunable quantum Hall edge conduction in bilayer graphene through spin-orbit interaction. *Phys. Rev. B* **98**, 115307 (2018).
14. Island, J. O. et al. Spin-orbit-driven band inversion in bilayer graphene by the van der Waals proximity effect. *Nature* **571**, 85–89 (2019).
15. Wang, D. et al. Quantum Hall effect measurement of spin-orbit coupling strengths in ultraclean bilayer graphene/ WSe_2 heterostructures. *Nano Lett.* **19**, 7028–7034 (2019).
16. Li, Y. & Koshino, M. Twist-angle dependence of the proximity spin-orbit coupling in graphene on transition-metal dichalcogenides. *Phys. Rev. B* **99**, 075438 (2019).
17. Zhang, Y. et al. Enhanced superconductivity in spin-orbit proximitized bilayer graphene. *Nature* **613**, 268–273 (2023).
18. Holleis, L. et al. Nematicity and orbital depairing in superconducting Bernal bilayer graphene. *Nat. Phys.* **21**, 444–450 (2025).
19. Li, C. et al. Tunable superconductivity in electron- and hole-doped Bernal bilayer graphene. *Nature* **631**, 300–306 (2024).
20. Chou, Y.-Z., Wu, F. & Das Sarma, S. Enhanced superconductivity through virtual tunneling in Bernal bilayer graphene coupled to WSe_2 . *Phys. Rev. B* **106**, L180502 (2022).
21. David, A., Rakyta, P., Kormányos, A. & Burkard, G. Induced spin-orbit coupling in twisted graphene-transition metal dichalcogenide heterobilayers: twistronics meets spintronics. *Phys. Rev. B* **100**, 085412 (2019).
22. Naimer, T., Zollner, K., Gmitra, M. & Fabian, J. Twist-angle dependent proximity induced spin-orbit coupling in graphene/transition metal dichalcogenide heterostructures. *Phys. Rev. B* **104**, 195156 (2021).
23. Zollner, K., João, S. M., Nikolić, B. K. & Fabian, J. Twist- and gate-tunable proximity spin-orbit coupling, spin relaxation anisotropy, and charge-to-spin conversion in heterostructures of graphene and transition metal dichalcogenides. *Phys. Rev. B* **108**, 235166 (2023).
24. Li, H. et al. Electrode-free anodic oxidation nanolithography of low-dimensional materials. *Nano Lett.* **18**, 8011–8015 (2018).
25. Masseroni, M. et al. Spin-orbit proximity in MoS_2 /bilayer graphene heterostructures. *Nat. Commun.* **15**, 9251 (2024).
26. Seiler, A. M. et al. Layer-selective spin-orbit coupling and strong correlation in bilayer graphene. Preprint at <https://arxiv.org/abs/2403.17140> (2024).
27. Sun, L. et al. Spin-orbit proximity in MoS_2 /bilayer graphene heterostructures. *Nat. Commun.* **14**, 3771 (2023).
28. McMillan, W. L. Transition temperature of strong-coupled superconductors. *Phys. Rev.* **167**, 331–344 (1968).
29. Allen, P. B. & Dynes, R. C. Transition temperature of strong-coupled superconductors reanalyzed. *Phys. Rev. B* **12**, 905–922 (1975).
30. Tolmachev, V. V. Logarithmic criterion for superconductivity. *Dokl. Akad. Nauk SSSR* **140**, 563–566 (1961).
31. Morel, P. & Anderson, P. W. Calculation of the superconducting state parameters with retarded electron-phonon interaction. *Phys. Rev.* **125**, 1263–1271 (1962).
32. Yankowitz, M. et al. Tuning superconductivity in twisted bilayer graphene. *Science* **363**, 1059–1064 (2019).
33. Kedves, M. et al. Stabilizing the inverted phase of a WSe_2 /BLG/ WSe_2 heterostructure via hydrostatic pressure. *Nano Lett.* **23**, 9508–9514 (2023).
34. McCann, E. & Koshino, M. The electronic properties of bilayer graphene. *Rep. Prog. Phys.* **76**, 056503 (2013).
35. Dong, Z., Davydova, M., Ogunnaike, O. & Levitov, L. Isospin- and momentum-polarized orders in bilayer graphene. *Phys. Rev. B* **107**, 075108 (2023).
36. Lin, J.-X. et al. Spontaneous momentum polarization and diodicity in Bernal bilayer graphene. Preprint at <https://arxiv.org/abs/2302.04261> (2023).
37. Nuckolls, K. P. et al. Quantum textures of the many-body wavefunctions in magic-angle graphene. *Nature* **620**, 525–532 (2023).
38. Kim, H. et al. Imaging inter-valley coherent order in magic-angle twisted trilayer graphene. *Nature* **623**, 942–948 (2023).
39. Arp, T. et al. Intervalley coherence and intrinsic spin-orbit coupling in rhombohedral trilayer graphene. *Nat. Phys.* **20**, 1413–1420 (2024).
40. Chatterjee, S., Wang, T., Berg, E. & Zaletel, M. P. Inter-valley coherent order and isospin fluctuation mediated superconductivity in rhombohedral trilayer graphene. *Nat. Commun.* **13**, 6013 (2022).
41. Koh, J. M., Thomson, A., Alicea, J. & Lantagne-Hurtubise, É. Symmetry-broken metallic orders in spin-orbit-coupled Bernal bilayer graphene. *Phys. Rev. B* **110**, 245118 (2024).
42. You, Y.-Z. & Vishwanath, A. Kohn-Luttinger superconductivity and intervalley coherence in rhombohedral trilayer graphene. *Phys. Rev. B* **105**, 134524 (2022).
43. Xie, M. & Das Sarma, S. Flavor symmetry breaking in spin-orbit coupled bilayer graphene. *Phys. Rev. B* **107**, L201119 (2023).
44. Thomson, A., Sorensen, I. M., Nadj-Perge, S. & Alicea, J. Gate-defined wires in twisted bilayer graphene: from electrical detection of intervalley coherence to internally engineered Majorana modes. *Phys. Rev. B* **105**, L081405 (2022).
45. Koh, J. M., Alicea, J. & Lantagne-Hurtubise, É. Correlated phases in spin-orbit-coupled rhombohedral trilayer graphene. *Phys. Rev. B* **109**, 035113 (2024).
46. Zhumagulov, Y., Kochan, D. & Fabian, J. Swapping exchange and spin-orbit induced correlated phases in proximitized Bernal bilayer graphene. *Phys. Rev. B* **110**, 045427 (2024).
47. Dong, Z., Lantagne-Hurtubise, É. & Alicea, J. Superconductivity from spin-canting fluctuations in rhombohedral graphene. Preprint at <https://arxiv.org/abs/2406.17036> (2024).
48. Frigeri, P. A., Agterberg, D. F., Koga, A. & Sigrist, M. Superconductivity without inversion symmetry: MnSi versus CePt_3Si . *Phys. Rev. Lett.* **92**, 097001 (2004).
49. Lu, J. M. et al. Evidence for two-dimensional Isuperconductivity in gated MoS_2 . *Science* **350**, 1353–1357 (2015).
50. Saito, Y. et al. Superconductivity protected by spin-valley locking in ion-gated MoS_2 . *Nat. Phys.* **12**, 144–149 (2016).

Publisher's note Springer Nature remains neutral with regard to jurisdictional claims in published maps and institutional affiliations.

Springer Nature or its licensor (e.g. a society or other partner) holds exclusive rights to this article under a publishing agreement with the author(s) or other rightsholder(s); author self-archiving of the accepted manuscript version of this article is solely governed by the terms of such publishing agreement and applicable law.

© The Author(s), under exclusive licence to Springer Nature Limited 2025

Article

Methods

Device fabrication

The majority of the fabrication processes follow the standard flake transfer and lithography explained in a previous study¹⁷. Here we focus on the interfacial twisting between BLG and WSe₂. Large flakes of BLG and WSe₂ are exfoliated on silicon dioxide/silicon) chips. The crystal orientation of WSe₂ can be identified by second harmonic generation⁵¹ (Extended Data Fig. 1b), where the polarization of the incident and reflected beams are selected to lie parallel to the scattering plane. The directions with maximized second harmonic generation signal correspond to the in-plane crystal orientations along the W–Se direction (armchair direction). BLG is somewhat trickier. We identify flakes with long straight edges forming angles that are multiple of 30°, for example, 3 edges form 2 angles of 150° in Extended Data Fig. 1c. The configuration is consistent with the assignment that the straight edges are along the zigzag- or armchair-edge direction of graphene. We then cut the large BLG flake into small pieces by atomic-force-microscope-actuated cutting²⁴ (Extended Data Fig. 1d). First, we picked up the topmost hexagonal boron nitride, the top graphite gate, the top hexagonal boron nitride dielectric and the large WSe₂ flake using propylene carbonate film on polydimethylsiloxane. Then, we aligned the straight edge of BLG with the crystal orientation of WSe₂ and controlled the approach of the propylene carbonate/polydimethylsiloxane stamp so that only one BLG piece was picked up. The silicon dioxide/silicon chip was manually rotated by an angle $\theta \approx 6^\circ$, and a second piece of BLG was picked up but not overlapping with the first one. The same processes were repeated for the remaining BLG pieces (Extended Data Fig. 1f,g). Depending on whether the BLG straight edge used for alignment is along the zigzag or armchair direction, the crystal axes of the six BLG pieces were rotated relative to the WSe₂ axis by an angle θ of 0°, 6°, 12°, 18°, 24° and 30° (armchair direction) or vice versa (zigzag direction). The two configurations can be distinguished by measuring the Ising SOC strengths of the devices at the two ends. The large (small) Ising device corresponds to about 0° (about 30°) alignment owing to the reflection symmetry^{16,20–22}. A typical finished stack is shown in Extended Data Fig. 1h; a series of different rotation angles between BLG and WSe₂ can be clearly seen from the optical image. The stack went through standard lithographic and etching processes for final device preparation (Extended Data Fig. 1i).

Measurements

All measurements were performed in a dilution refrigerator (Oxford Triton) with a base temperature of about 30 mK and a 1T/1T/9T (XYZ) superconducting vector magnet, using standard low-frequency lock-in amplifier techniques. Unless otherwise specified, measurements were taken at the base temperature. Frequencies of the lock-in amplifiers (Stanford Research, models 865a) were kept in the range of 7–40 Hz to reduce the electronic noise and measure the device's d.c. properties. The a.c. excitation was kept below 5 nA; most measurements were taken at 1 nA to preserve the linearity of the system and to avoid disturbing the fragile states at low temperatures. Each of the d.c. fridge lines passed through cold filters, including 4 Pi filters that filter out a range from about 80 MHz to >10 GHz, as well as a two-pole RC (resistor–capacitor) low-pass filter.

Reproducibility of twist-programmable superconductivity

Supplementary Figs. 1–3 show the data measured from three sets of moiréless twisting devices (D1–D3), with the corresponding devices marked by the labels in the optical images. θ -modulated Ising SOC and superconductivity are well reproduced from all the three sets of devices. Within each set, we see a clear trend that superconductivity onsets at a lower D field for the device with low Ising SOC and gradually onsets at a higher D field for the device with large

Ising SOC. Accordingly, Ising SOC strength evolves as a function of twist angle θ . The θ -dependent Ising SOC strengths are summarized in Fig. 1e: the magnitude of proximitized Ising SOC is large within a broad angle range, and is quickly suppressed when $\theta = 20^\circ$ –30°. Specially, the first device in the device set D2 (Supplementary Fig. 2a; see also Supplementary Fig. 4) appears to have a minimal Ising SOC, and superconductivity does not appear at zero magnetic field. The device is consistent with the scenario that the alignment between BLG and WSe₂ is $\theta \approx 30^\circ$.

Quantifying Ising SOC

One way to quantify the WSe₂-induced Ising SOC $H_i = \frac{1}{2}\lambda_i\tau_zs_z$ (λ_i is the Ising SOC strength in the main text; here τ_z and s_z are the Pauli matrices corresponding to valley and spin degree of freedom) is to probe the octet zeroth Landau level in BLG. It is noted that these Landau-level energies are not sensitive to Rashba SOC¹³. The sets of two Landau levels that cross at filling factors $v = \pm 3$ have opposite layer polarizations, so that their energy difference (at zero D field) is given by $\Delta E = E_Z \pm \lambda_i/2$ (E_Z is the Zeeman gap between spin-up and spin-down Landau levels). Therefore, the critical field B_{\perp}^* that makes ΔE vanish is $2E_Z = 2g\mu_B B_{\perp}^* = \lambda_i$ (here, g -factor value $g = 2$ is used and μ_B is the Bohr magneton, see also Supplementary Fig. 10a–f). However, this method does not work when λ_i is negative as the energy-level crossing is not inverted¹⁵.

Independently, $|\lambda_i|$ can also be extracted from the doping-dependent FFT splitting of the quantum oscillations, regardless the sign of λ_i (Fig. 1f–i and Extended Data Fig. 2a). Extended Data Fig. 2b,c shows the doping-dependent FFT splitting B_{split} measured within the non-interacting phase (schematics in Fig. 1h,i) at different D fields and at higher doping densities (that is, away from the van Hove singularities). Ising-type splitting is suppressed with increasing $|n|$, in contrast to the Rashba-type splitting which increases with increasing $|n|$ (ref. 17). The detailed mapping of B_{split} as a function of n and D enables comparison with single-particle band-structure calculation (Supplementary Information section 1) that quantifies the Ising-induced Fermi-surface imbalance. The dashed lines in Extended Data Fig. 2b,c are calculated frequency splittings for $|\lambda_i| \approx 1.4$ meV (Extended Data Fig. 2b) and $|\lambda_i| \approx 0.4$ meV (Extended Data Fig. 2c), respectively. Both cases roughly match the experimental data. The overall trend is that (1) at constant $|\lambda_i|$, higher D features larger B_{split} and (2) at constant D , higher $|\lambda_i|$ features larger B_{split} . The observed trends put strong constraints on the estimates of the Ising SOC strength.

It is noted that one single Ising SOC strength provides a good fit to the data at different D fields (from $D/\epsilon_0 = 0.2$ V nm^{−1} to $D/\epsilon_0 = 1$ V nm^{−1}; Extended Data Fig. 2b), suggesting that Ising SOC is already maximal at $D/\epsilon_0 = 0.2$ V nm^{−1} and larger D values do not further increase the Ising SOC strength. For Ising extraction, frequency analysis at a finite D field and higher doping (that is, away from the van Hove singularities) is more accurate compared with the zero D case for the following reasons: (1) Ising-induced splitting is suppressed at the zero D limit (Supplementary Fig. 11), which makes it difficult to precisely quantify by comparing with the single-particle band structure (grey dashed line in Extended Data Fig. 2b); and (2) the effective Rashba SOC is more pronounced⁵² at $D/\epsilon_0 = 0$ V nm^{−1} owing to reduced sublattice and layer polarizations, which further complicates the analysis (Supplementary Information section 1 and Supplementary Fig. 16). The evolution of the effective Rashba SOC is plotted in Supplementary Fig. 16. We find that for moderate values of interlayer potential difference ($U > 15$ meV), the microscopic Rashba SOC induced by WSe₂ becomes strongly suppressed, consistent with the experiment.

Supplementary Fig. 10a–f shows the Landau-level crossing for $v = \pm 3$ and Supplementary Fig. 10g shows the corresponding quantum oscillation frequencies within the non-interacting Ising symmetry-breaking phase. Both methods return $|\lambda_i| \approx 1.6$ meV, validating the quantum oscillation method in the paper.

Principles for FFT analysis

Correctly identifying the quantum oscillation frequencies is critical for figuring out the type and the number of Fermi pockets for each flavour-polarized phases. Here we summarize basic principles for FFT analysis, applying them to FP(2, 2, 2) and FP(1, 3, 1).

1. To identify the intrinsic Fermi-surface frequencies, we want to work on FFT analysis with B_{\perp} range as low as possible. At slightly higher B_{\perp} , magnetic breakdown⁵³ kicks in as B_{\perp} -assisted electron tunnelling between different Fermi surfaces. Consequently, the most pronounced frequencies might be a sum (or difference) of two base frequencies instead of the intrinsic ones.
2. Follow the sum rule that all the intrinsic frequencies with their multiplications add up to 1. The multiplications return the number of Fermi pockets for each type. Looking at the doping dependence of f_v , if one frequency $f_v^{(1)}$ decreases versus doping, it is guaranteed that there is another frequency that evolves reversely. One pocket shrinks while some other pockets grow.
3. We check for the evolution of phase diagram as a function of D fields and doping n . Some FFT frequencies continuously evolve in the n - D phase space, which provides further guidance for the neighbouring correlated phases.

Identification of FP(2, 2, 2) phase

Ultrahigh-resolution quantum oscillations at high D fields allow for resolving subtle symmetry-breaking Fermi pockets. Looking carefully at the FFT frequency $f_v^{(2)}$ in Extended Data Figs. 5b and 6b,d, $f_v^{(2)}$ decreases monotonically with lowering doping until reaching $n \approx -8.25 \times 10^{11} \text{ cm}^{-2}$ for $D/\epsilon_0 = 1.265 \text{ V nm}^{-1}$ ($n \approx -7.2 \times 10^{11} \text{ cm}^{-2}$ for $D/\epsilon_0 = 1.2 \text{ V nm}^{-1}$), beyond which the dependence of $f_v^{(2)}$ is flattened whereas $f_v^{(1)}$ keeps increasing throughout. This indicates that the sum rule $2f_v^{(1)} + 4f_v^{(2)} \approx 1$ of the FP(2, 4) phase at higher doping is no longer satisfied for lower dopings, suggesting an altered Fermi-surface structure. Indeed, measuring quantum oscillations to higher B_{\perp} field reveals the emergence of a third very low frequency around the phase boundary as marked by the green arrows in Extended Data Fig. 7. The FFT data shown in Extended Data Figs. 5b and 6b,d clearly reveal the third frequency $f_v^{(3)}$ growing rapidly from zero at the phase boundary to a value matching $f_v^{(2)}$ at slightly higher doping. The frequencies obey $2f_v^{(1)} + 2f_v^{(2)} + 2f_v^{(3)} \approx 1$, as discussed in the main text corresponding to an additional symmetry breaking with trigonally warped pockets of two sizes $f_v^{(2)}$ and $f_v^{(3)}$.

Identification of FP(1, 3, 1) phase

The identification of the FP(1, 3, 1) phase is more subtle, involving extensive quantum oscillation measurements. The raw data (Extended Data Fig. 7a,b; $n \approx -6.6 \times 10^{11} \text{ cm}^{-2}$ to $n \approx -5.3 \times 10^{11} \text{ cm}^{-2}$ taken at $D/\epsilon_0 \approx 1.2 \text{ V nm}^{-1}$) reveal 3 oscillation frequencies. A high frequency marked $f_v^{(4)}$ appears clearly. At really low $B_{\perp} \approx 0.05 \text{ T}$, a relatively low frequency called $f_v^{(6)}$ onsets. Further increasing B_{\perp} , each $f_v^{(6)}$ period splits into four, giving rise to $f_v^{(5)}$, which is indeed roughly four times the frequency $f_v^{(6)}$ (Extended Data Fig. 7c).

It is natural to ask whether $f_v^{(5)}$ is simply a higher (fourth) harmonic of $f_v^{(6)}$. This can be answered by the measurements at low D fields in the same phase region (Extended Data Figs. 8 and 9). Frequencies are marked by arrows. When lowering the D fields, $f_v^{(4)}$ gradually increases, whereas $f_v^{(5)}$ and $f_v^{(6)}$ gradually decrease. At $D/\epsilon_0 = 1 \text{ V nm}^{-1}$ (Extended Data Fig. 8b,d,f), $f_v^{(5)}$ already deviates from being four times the value of $f_v^{(6)}$. Eventually at $D/\epsilon_0 = 0.85 \text{ V nm}^{-1}$ (Extended Data Fig. 8a,c,e), the frequency $f_v^{(6)}$ completely disappears whereas $f_v^{(5)}$ independently survives. This D evolution of the two frequencies ($f_v^{(5)}$ and $f_v^{(6)}$) supports their independence. Meanwhile at $D/\epsilon_0 = 0.85 \text{ V nm}^{-1}$, the existing 2 frequencies ($f_v^{(4)}$ and $f_v^{(5)}$) obey $f_v^{(4)} + 3f_v^{(5)} \approx 1$; we denote the flavour-polarized phase at this D field as FP(1, 3). The above D -field evolution indicates that the FP(1, 3, 1)

phase at high D develops from the FP(1, 3) phase at low D as D is increased.

After establishing the existence of three frequencies, we comment on the number of pockets for each type. This relies on the correct identification of intrinsic Fermi-surface frequencies and their harmonics. At slightly higher B_{\perp} , magnetic breakdown⁵³ kicks in as B_{\perp} -assisted electron tunnelling between different Fermi surfaces. Consequently, the pronounced frequencies might be a sum (or difference) of two base frequencies instead of the intrinsic ones. This is the case for FP(1, 3) and FP(1, 3, 1) phase. Extended Data Fig. 8c shows the normalized FFT from quantum oscillations going up to $B_{\perp} = 0.45 \text{ T}$. The frequency peak at $f_v \approx 0.75$ is stronger than the one at $f_v \approx 0.6$ (marked by the arrow). However, the relative intensity changes by reducing the B_{\perp} range to 0.23 T (Extended Data Fig. 10a). At this condition, the peak at $f_v \approx 0.6$ is stronger than the one at $f_v \approx 0.75$, suggesting that the one marked by the arrow ($f_v \approx 0.6$ in Extended Data Fig. 10a) is the intrinsic frequency; the one at $f_v \approx 0.75$ is instead a sum harmonic $f_v^{(4)} + f_v^{(5)}$. By identifying the intrinsic high frequency $f_v^{(4)}$, one obtains $f_v^{(4)} + 3f_v^{(5)} \approx 1$, indicating 1 large and 3 small Fermi surfaces, that is, FP(1, 3). A similar situation holds for the other D fields, such as at $D/\epsilon_0 = 1.2 \text{ V nm}^{-1}$ (Extended Data Figs. 9c and 10c), where we find $f_v^{(4)} + 3f_v^{(5)} + f_v^{(6)} \approx 1$.

Inter-valley coherence

The occurrence of superconducting state SC₃ in the symmetry-breaking state FP(1, 3, 1) strongly indicates the inter-valley coherent nature of FP(1, 3, 1). Focusing on the single largest Fermi pocket ($f_v^{(4)}$) that is non-degenerate, there are two options: it is either valley-polarized and therefore breaks time-reversal symmetry, or it is inter-valley coherent. Coherence between the K and K' valleys would restore time-reversal symmetry for the largest Fermi pocket, naturally more susceptible to pairing. It is noted that in moiré graphene, it is established that superconductivity originates from an inter-valley-coherent order^{37,38}.

Independent evidence for inter-valley coherence comes from analysing the evolution of phase boundaries as a function of B_{\perp} . An out-of-plane magnetic field B_{\perp} favours valley-polarized states that are characterized by large orbital moments. As the B_{\perp} field is increased, valley-polarized states with large orbital moments are expected to take over more of the phase space compared with valley-balanced states³⁹. The evolution of the phase boundaries with B_{\perp} can be clearly identified from quantum oscillations (Extended Data Fig. 11). Here, the lowest doping density range ($n > -3 \times 10^{11} \text{ cm}^{-2}$) corresponds to a spin-valley-locked FP(6) phase¹⁷. Within this phase, the K and K' valleys are equally populated with opposite spins, resulting in zero net orbital moment. At the doping density $-3 \times 10^{11} \text{ cm}^{-2} > n > -4.3 \times 10^{11} \text{ cm}^{-2}$, the oscillation frequency peaks at $f_v = 1$ indicating an FP(1) phase. The phase space shows a rich evolution: a phase transition develops with increasing B_{\perp} , consistent with a spin-valley-polarized FP(1) (red line in Extended Data Fig. 11b) emerging when B_{\perp} is applied. Importantly, at the lowest B_{\perp} ($B_{\perp} \approx 0 \text{ T}$), the phase boundary between FP(1) and FP(6) (black dashed line at $n \approx -3 \times 10^{11} \text{ cm}^{-2}$) does not move with B_{\perp} , suggesting that the FP(1) at $B_{\perp} \approx 0 \text{ T}$ is characterized by coherence between the two valleys (over the spin-valley-polarized phase), so that the orbital moments cancel. The same logic applies to the other symmetry-breaking phases at slightly higher doping. A large FFT frequency dominates at $f_v > 1/2$ whereas the phase boundaries persist in doping without moving when B_{\perp} is applied, suggesting the existence of one large Fermi pocket with diminished or no orbital moments and hence inter-valley coherence for FP(1, 3, 1).

Sample alignment with in-plane magnetic field

In-plane-field measurements were performed by mounting the sample vertically with a homemade frame to access $B_{\parallel} > 1 \text{ T}$. A small B_{\perp} component is inevitably introduced when B_{\parallel} is applied owing to imperfect vertical sample alignment. The B_x and B_y directions of the vector magnet are used to compensate the B_{\perp} component. The compensation is crucial

Article

for the measurements of large Pauli-limit violation of SC_3 , because at $B_{\parallel} = 7 \text{ T}$ or so, an out-of-plane component $B_{\perp} \approx 0.1\text{--}0.2 \text{ mT}$ almost completely suppresses the superconductivity. In addition, the cancellation of B_{\perp} gives an accurate R_{xx} dependence on B_{\parallel} and temperature so that the extraction of α in Fig. 4 is reliable.

Multiband superconductivity analysis

We consider an electronic system with two bands, with an additional (spin) degree of freedom in each band. The mean-field ansatz for the simplest order parameter is a vector form owing to the multiband structure

$$\Delta = \hat{g}_{\text{initial}} \left\langle \begin{pmatrix} \frac{1}{\Omega} \sum_{\mathbf{k}} \psi_{\mathbf{k}1+} \psi_{\mathbf{k}1-} \\ \frac{1}{\Omega} \sum_{\mathbf{k}} \psi_{\mathbf{k}2+} \psi_{\mathbf{k}2-} \end{pmatrix} \right\rangle, \quad (1)$$

where, \hat{g}_{initial} is a matrix of repulsive interaction from the intrinsic Coulomb interaction, Ω is the system volume, $\psi_{\mathbf{k},n,p}$ annihilates an electron with momentum \mathbf{k} , in band $n = 1, 2$, and internal flavour $p = \pm$.

We introduce an energy scale ω^* , below which the pairing interaction is activated. In the path-integral formalism, one integrates out the electrons with energy greater than ω^* , obtaining a renormalized, Tolmachev, Anderson and Morel (TAM) interaction matrix

$$\hat{g}_{\text{TAM}}(\omega^*) = \left[(\hat{g}_{\text{initial}})^{-1} + \begin{pmatrix} \ell_1 & \\ & \ell_2 \end{pmatrix} \right]^{-1}, \quad (2)$$

where $\ell_n = \left\{ \int_{\omega^*}^{\infty} + \int_{-\infty}^{-\omega^*} \right\} d\xi \frac{\mathcal{N}_n(\xi)}{|\xi|}$, and $\mathcal{N}_n(\xi)$ is the DOS of the n band at a distance ξ away from the Fermi level.

We define a multiband generalization of the superconducting pseudopotential

$$\mu_{\text{multi}}^* = \sqrt{\det \hat{g}_{\text{TAM}}(\omega^*)}. \quad (3)$$

We note that by setting interband interactions to zero, one simply obtains a diagonal \hat{g}_{TAM} matrix, with the appropriate single-band pseudopotentials $\mu_{1,2}^*$ on its diagonal. Investigation of μ_{multi}^* is motivated by the fact that a superconducting transition is associated with a singularity of the \hat{g} matrix emerging at an approximately T_c energy scale.

Predictions of conventional depairing mechanisms for SC_1 , SC_2 and SC_3

Here we summarize the main findings resulting from the conventional depairing mechanisms in the context of SC_1 , SC , and SC_3 , within the Ising superconductor framework^{17,48–50}. For SC_2 , we find that experimentally determined values of α are not well reproduced by realistic values of $\lambda_R \lesssim 10 \text{ meV}$ (Supplementary Information section 8). More precisely, conventional depairing theory would predict higher resilience (lower α by almost an order of magnitude) to the in-plane magnetic field. For the case of SC_1 , we find that the conventional depairing theory applies well, explaining the large PVR. As such, another mechanism, such as the interband-interaction scenario in the main text, must account for the relatively minor PVR in SC_2 . The direction of B_{\parallel} can further shed light on the depairing mechanism. Theoretically, SC_1 is not sensitive to the in-plane field direction, as reported previously in ref. 18.

For SC_2 , because both FP(2, 4) and FP(2, 2, 2) break the C_3 symmetry, we anticipate a dependence of T_c (or α) as the direction of B_{\parallel} is rotated. Experimentally, however, SC_2 shows no significant variation in T_c as the magnetic field is rotated (Supplementary Fig. 12), suggesting that this simple depairing picture relying on rigid occupancy of the trigonal-warping pockets should be revisited with a self-consistent Hartree–Fock pairing analysis, where the Fermi surfaces adjust in response to the magnetic field. Finally, we also highlight that the mechanism discussed in the main text, the modification of interband and intraband interactions with an in-plane magnetic field, is entirely independent of the field direction. This is in accordance with the experimental observations, yet contrasts with the ‘conventional’ depairing analysis.

Data availability

The data shown in the main figures are available from the CaltechDATA (<https://doi.org/10.22002/pcmle-qe565>). Other data that support the findings of this study are available from the corresponding authors upon reasonable request.

Code availability

The code that supports the findings of this study is available from the corresponding authors upon reasonable request.

51. Seyler, K. L. et al. Electrical control of second-harmonic generation in a WSe₂ monolayer transistor. *Nat. Nanotechnol.* **10**, 407–411 (2015).
52. Szentpéteri, B. et al. Tuning the proximity induced spin–orbit coupling in bilayer graphene/WSe₂ heterostructures with pressure. Preprint at <https://arxiv.org/abs/2409.20062> (2024).
53. Cohen, M. H. & Falicov, L. M. Magnetic breakdown in crystals. *Phys. Rev. Lett.* **7**, 231–233 (1961).

Acknowledgements We thank J. Alicea, É. Lantagne-Hurtubise, Z. Dong, A. Thomson, D. V. Chichinadze, A. Young and E. Berg for discussions. This work has been primarily supported by the Office of Naval Research (grant number N142112635). S.N.-P. and D.H. acknowledge the support of the Institute for Quantum Information and Matter, an NSF Physics Frontiers Center (PHY-2317110). Part of the measurements were supported by the Moore foundation (award 12967). We gratefully acknowledge the critical support and infrastructure provided for this work by The Kavli Nanoscience Institute at Caltech. G.S. acknowledges support from the Walter Burke Institute for Theoretical Physics at Caltech, and from the Yad Hanadiv Foundation through the Rothschild fellowship. H.M. and C.L. were supported by start-up funds from Florida State University and the National High Magnetic Field Laboratory. The National High Magnetic Field Laboratory is supported by the National Science Foundation through NSF/DMR-2128556 and the State of Florida. Y.O. and F.v.O. acknowledge support by Deutsche Forschungsgemeinschaft through CRC 183 (project C02). F.v.O was further supported by Deutsche Forschungsgemeinschaft through a joint ANR-DFG project (TWISTGRAPH).

Author contributions Y.Z. and S.N.-P. designed the experiment. Y.Z. fabricated the devices, performed the measurements and analysed the data. C.W.S. and A.M. helped with the measurements. Y.H. and D.H. performed the second harmonic generation measurements. G.S., H.M., C.L., F.v.O. and Y.O. developed the theoretical models and performed calculations. K.W. and T.T. provided the hexagonal boron nitride crystals. S.N.-P. supervised the project. Y.Z., G.S., C.L., F.v.O., Y.O. and S.N.-P. wrote the paper with the input of other authors.

Competing interests The authors declare no competing interests.

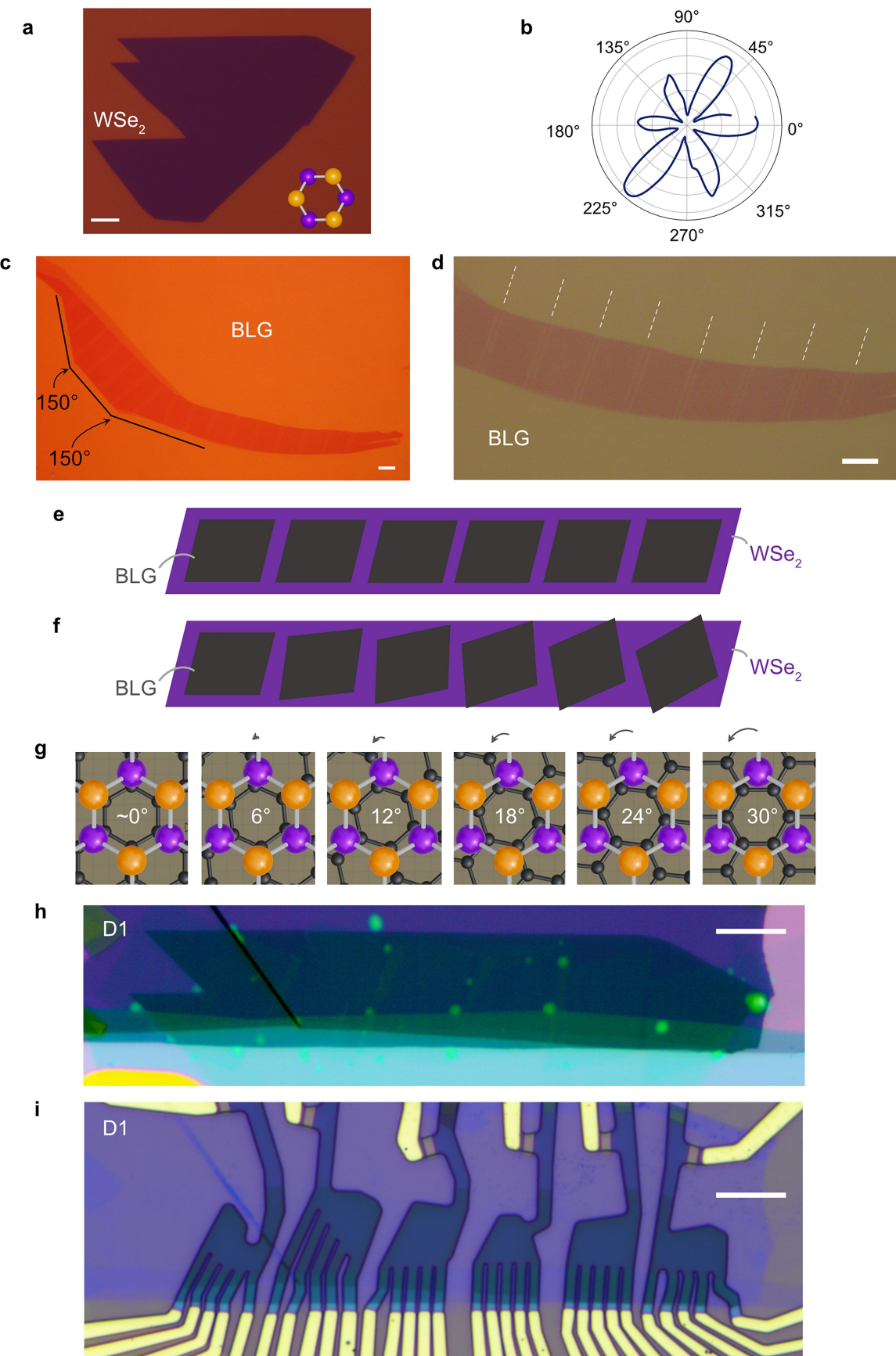
Additional information

Supplementary information The online version contains supplementary material available at <https://doi.org/10.1038/s41586-025-08959-3>.

Correspondence and requests for materials should be addressed to Yiran Zhang or Stevan Nadj-Perge.

Peer review information *Nature* thanks Shubhayu Chatterjee, Anna Seiler and the other, anonymous, reviewer(s) for their contribution to the peer review of this work.

Reprints and permissions information is available at <http://www.nature.com/reprints>.

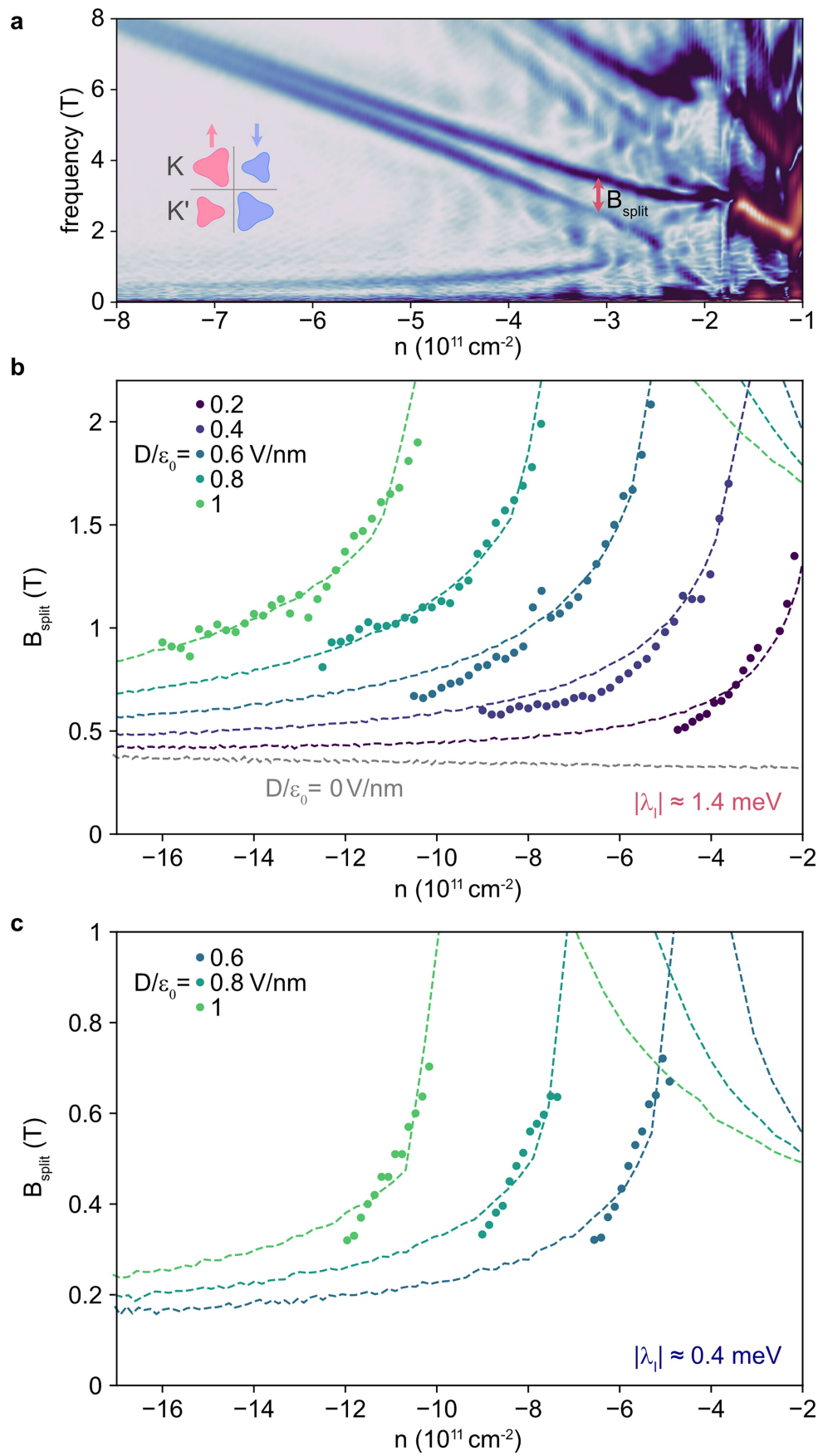


Extended Data Fig. 1 | See next page for caption.

Article

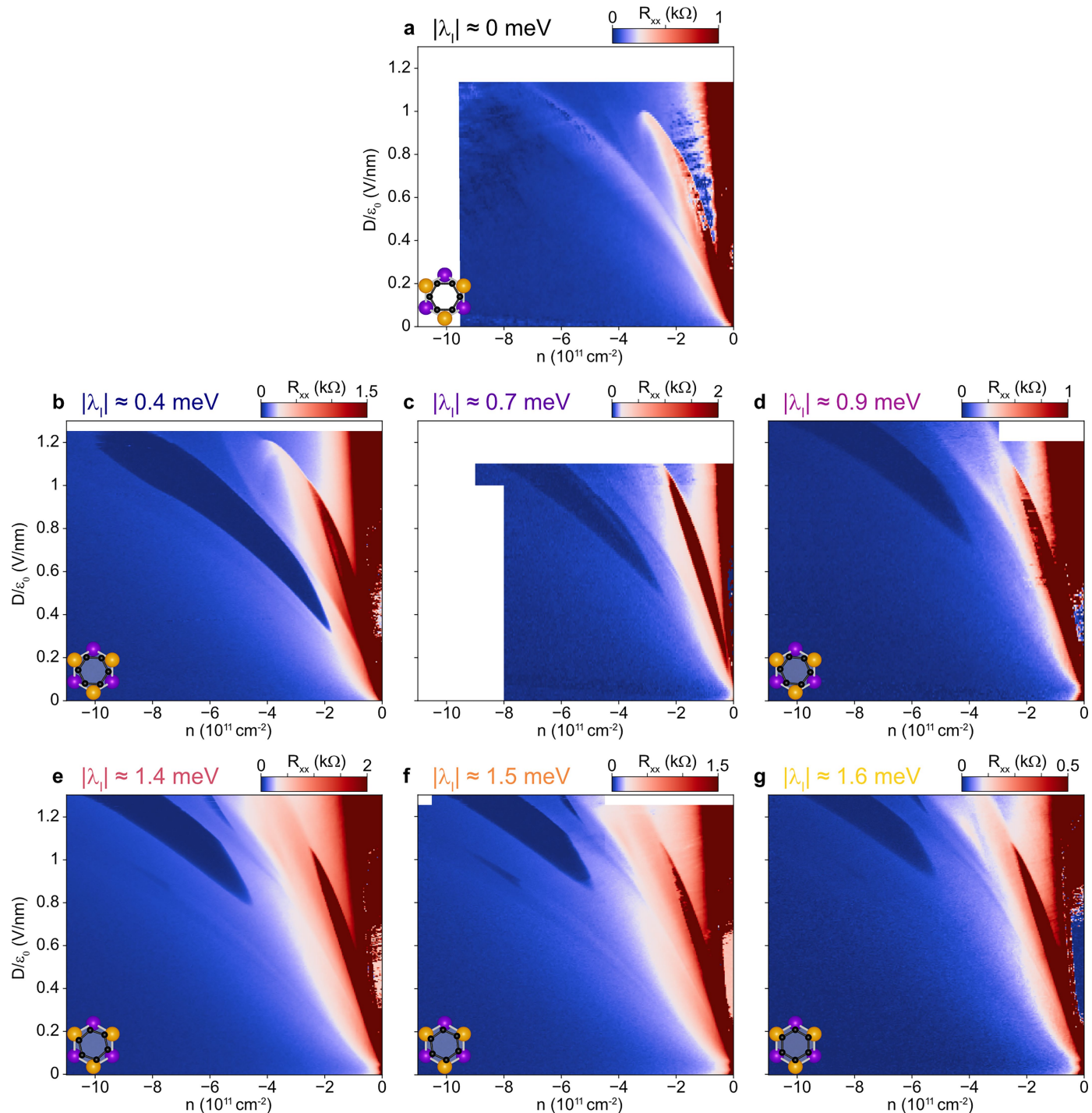
Extended Data Fig. 1 | Device fabrication for BLG-WSe₂ twisting. **a**, Optical image of a WSe₂ crystal. **b**, Second harmonic generation for the WSe₂ flake shown in **a**; the polarization of the incident and reflected beams are selected to lie parallel to the scattering plane. **c**, Optical image of a large BLG flake. Straight edges form angles 150° that are consistent with the three straight edges being along zigzag- or armchair-edge direction. **d**, Zoom-in image of the BLG in **c**, showing small BLG pieces that are separated by atomic-force-

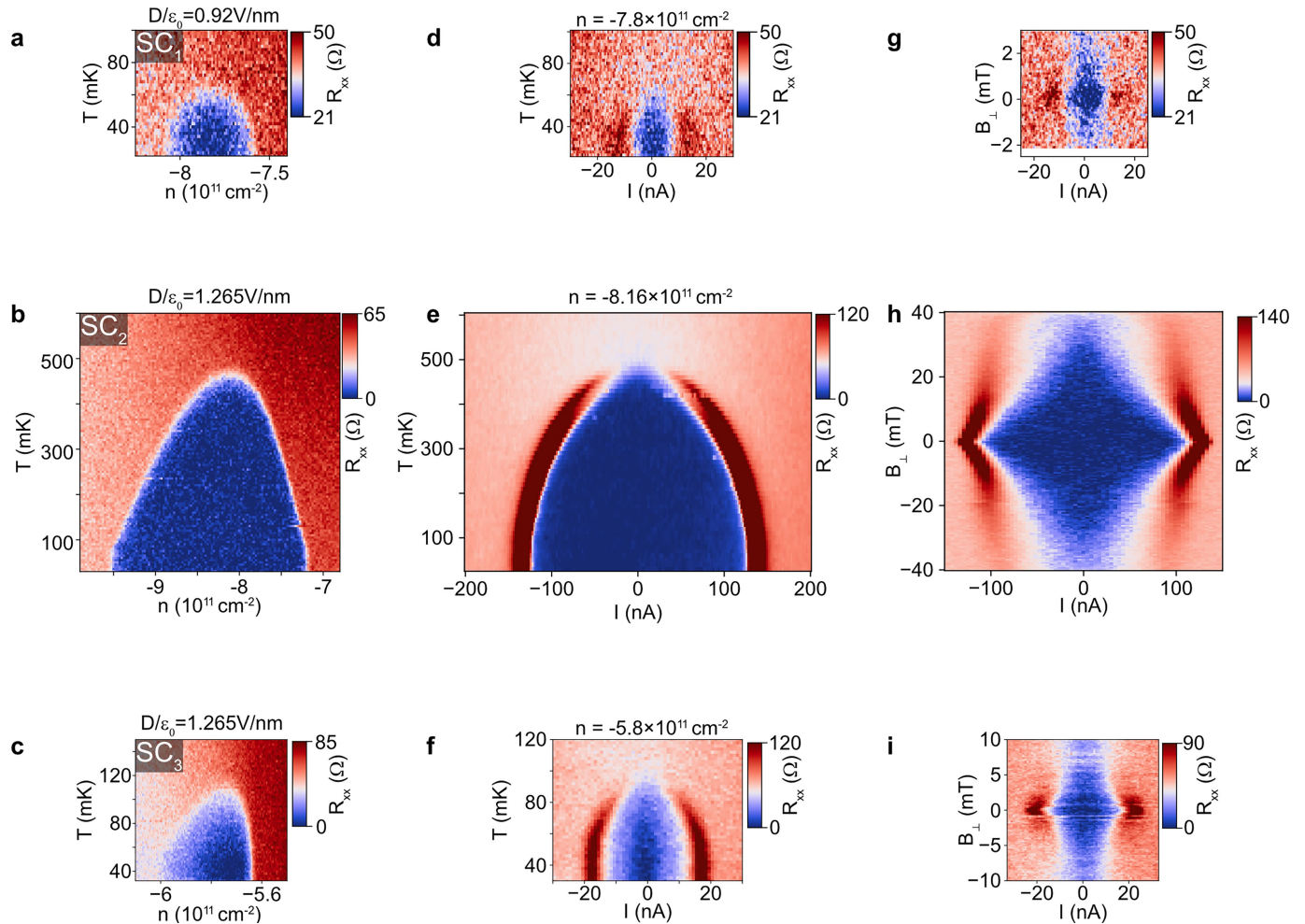
microscope-actuated cutting. **e-g**, Schematics showing the flake transferring processes for the continuous interfacial twisting. The BLG pieces are sequentially picked up with angles relative to WSe₂ in increments of 6°, from -0° to 30°. **h**, Optical image of the twisting stack, clearly showing that the BLG pieces form different twist angles relative to the WSe₂ crystal. **i**, Optical image of the finished device set D1. All the scale bars correspond to 10 μm.



Extended Data Fig. 2 | Quantifying Ising SOC strength $|\lambda_i|$ by quantum oscillations. **a**, The same data as the one in Fig. 1h, but without the frequency normalization to show B_{split} . **b,c**, Experimental (dots) doping-dependent frequency splitting around $\nu = 1/4$ measured at different D fields for a large

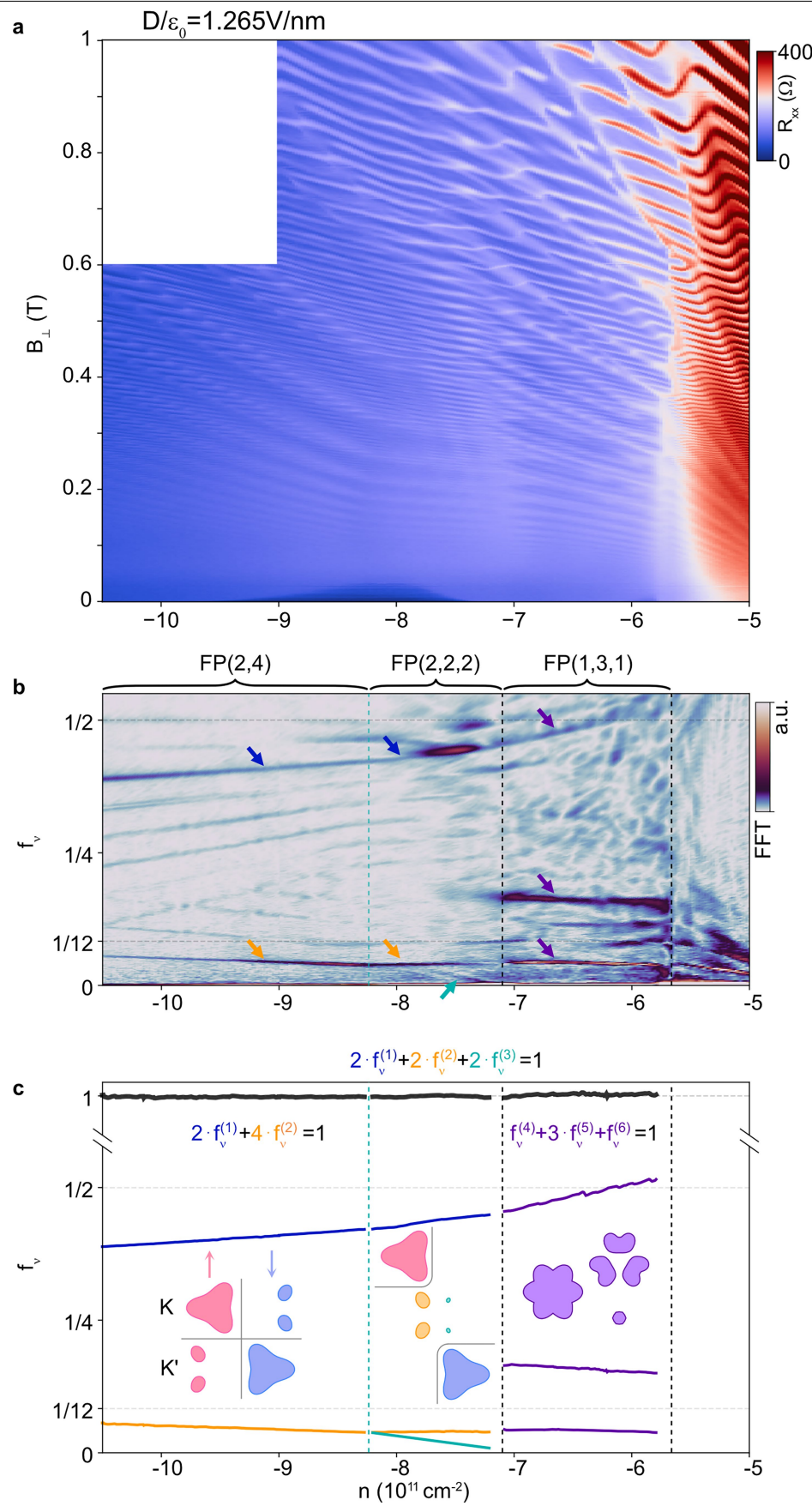
Ising device (**b**; $|\lambda_i| \approx 1.4 \text{ meV}$) and a small Ising device (**c**; $|\lambda_i| \approx 0.4 \text{ meV}$). The dashed lines are B_{split} calculated from single-particle band structure using the corresponding Ising SOC values. The gray dashed line in **b** corresponds to the frequency splitting at zero displacement field.





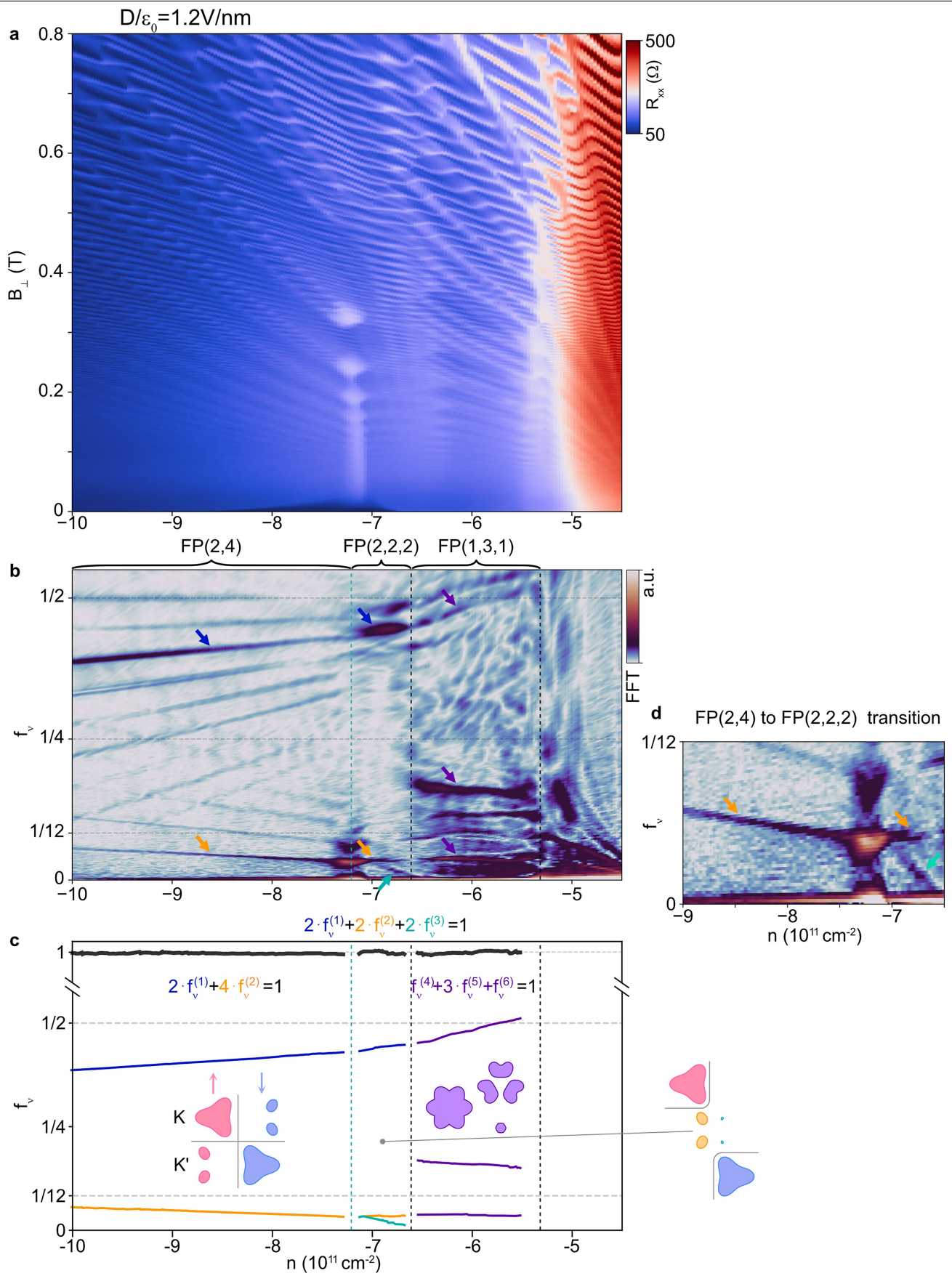
Extended Data Fig. 4 | Characterizations of the three superconducting regions \mathbf{SC}_1 , \mathbf{SC}_2 , and \mathbf{SC}_3 . **a-c**, Temperature dependence of the three superconducting domes \mathbf{SC}_1 (**a**), \mathbf{SC}_2 (**b**), and \mathbf{SC}_3 (**c**), respectively. **d-f**, Critical

current versus temperature at the corresponding D and n . **g-i**, Critical current disappearing with B_\perp at the same D and n as in **d-f**.



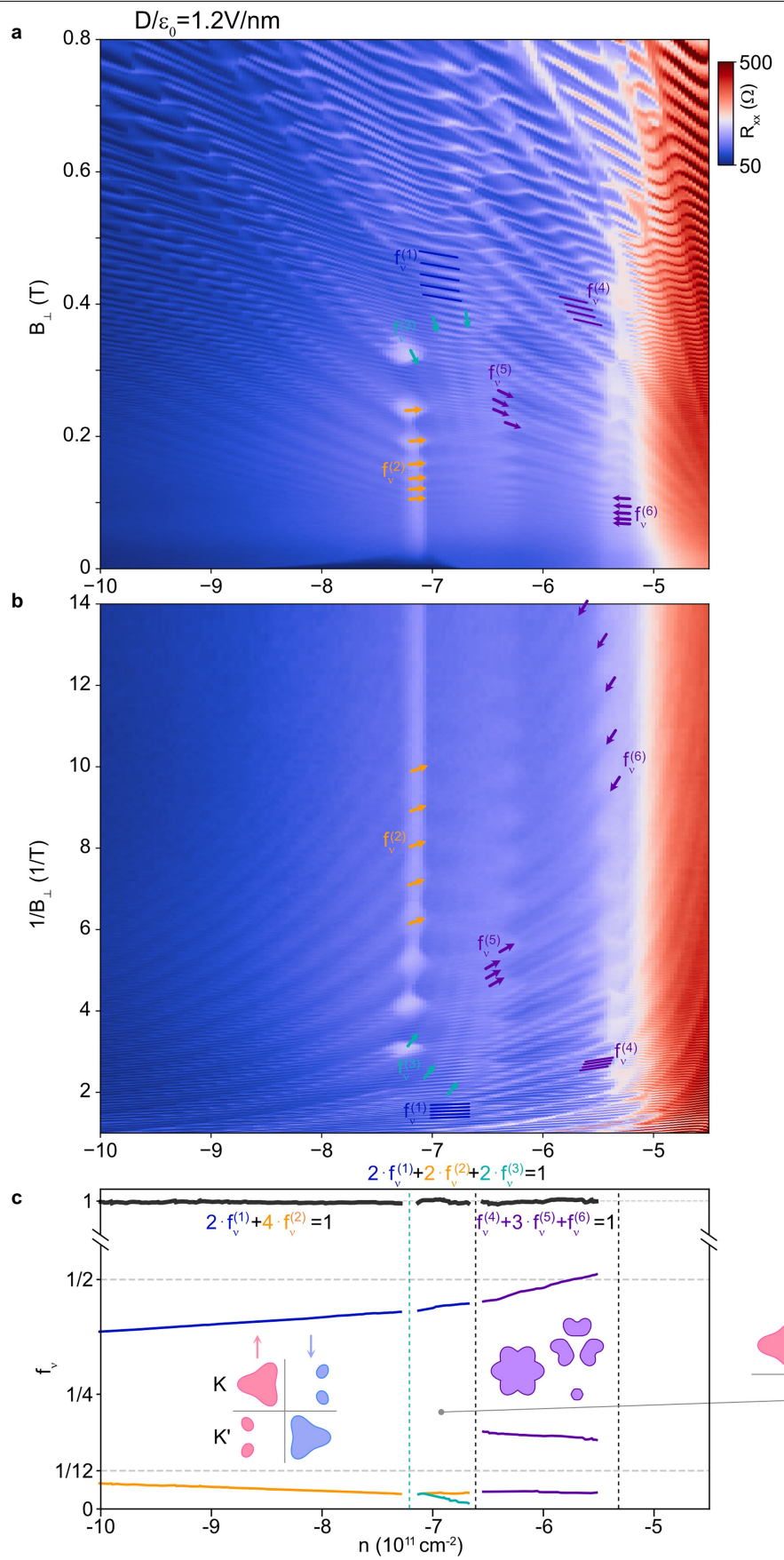
Extended Data Fig. 5 | Quantum oscillations and FFT measured at $D/\epsilon_0 = 1.265 \text{ V/nm}$. **a**, R_{xx} versus out-of-plane magnetic field B_\perp and doping density n measured at $D/\epsilon_0 = 1.265 \text{ V/nm}$ for a device with $|\lambda_i| \approx 1.5 \text{ meV}$.

b, Frequency-normalized Fourier transform of $R_{xx}(1/B_\perp)$ (using data within $0.05 < B_\perp < 0.8 \text{ T}$ to resolve $f_v^{(3)}$) over the same doping density range as in **a**. **c**, Intensity peaks in f_v from **b**.



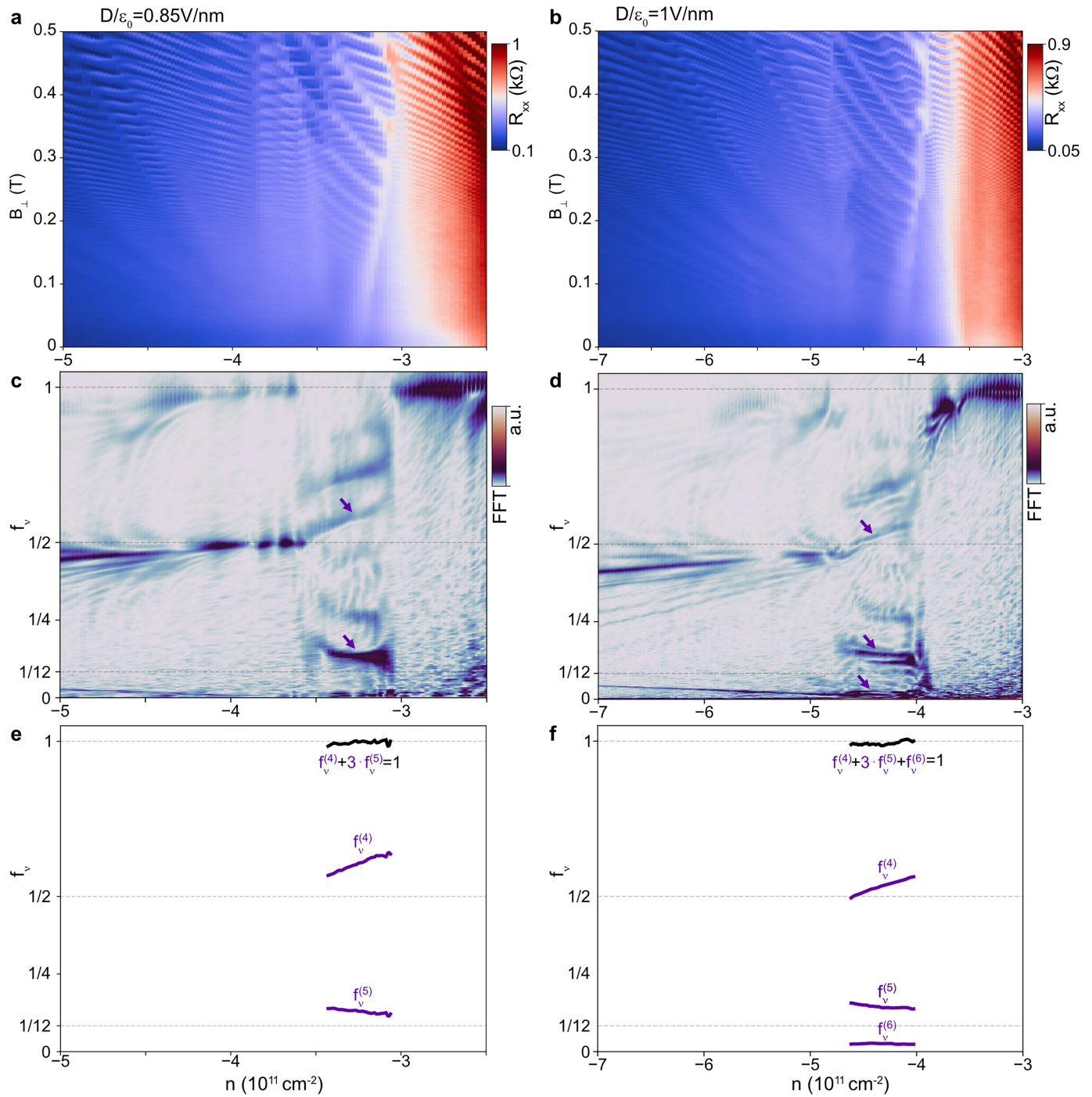
Extended Data Fig. 6 | Quantum oscillations and FFT measured at $D/\epsilon_0 = 1.2 \text{ V/nm}$. **a**, R_{xx} versus out-of-plane magnetic field B_\perp and doping density n measured at $D/\epsilon_0 = 1.2 \text{ V/nm}$ for a device with $|\lambda_i| \approx 1.5 \text{ meV}$.

b, Frequency-normalized Fourier transform of $R_{xx}(1/B_\perp)$ (using data within $0.05 < B_\perp < 0.8 \text{ T}$ to resolve $f_v^{(3)}$) over the same density range as in **a**. **c**, Intensity peaks in f_v from **b**. **d**, zoom-in image at low frequencies from **b**.



Extended Data Fig. 7 | Identifying FP(2,2,2) and FP(1,3,1) frequencies from the raw data. **a**, R_{xx} versus out-of-plane magnetic field B_\perp and doping density n measured at $D/\epsilon_0 = 1.2 \text{ V/nm}$ for a device with $|\lambda_l| \approx 1.5 \text{ meV}$. **b**, The same data as in **a**,

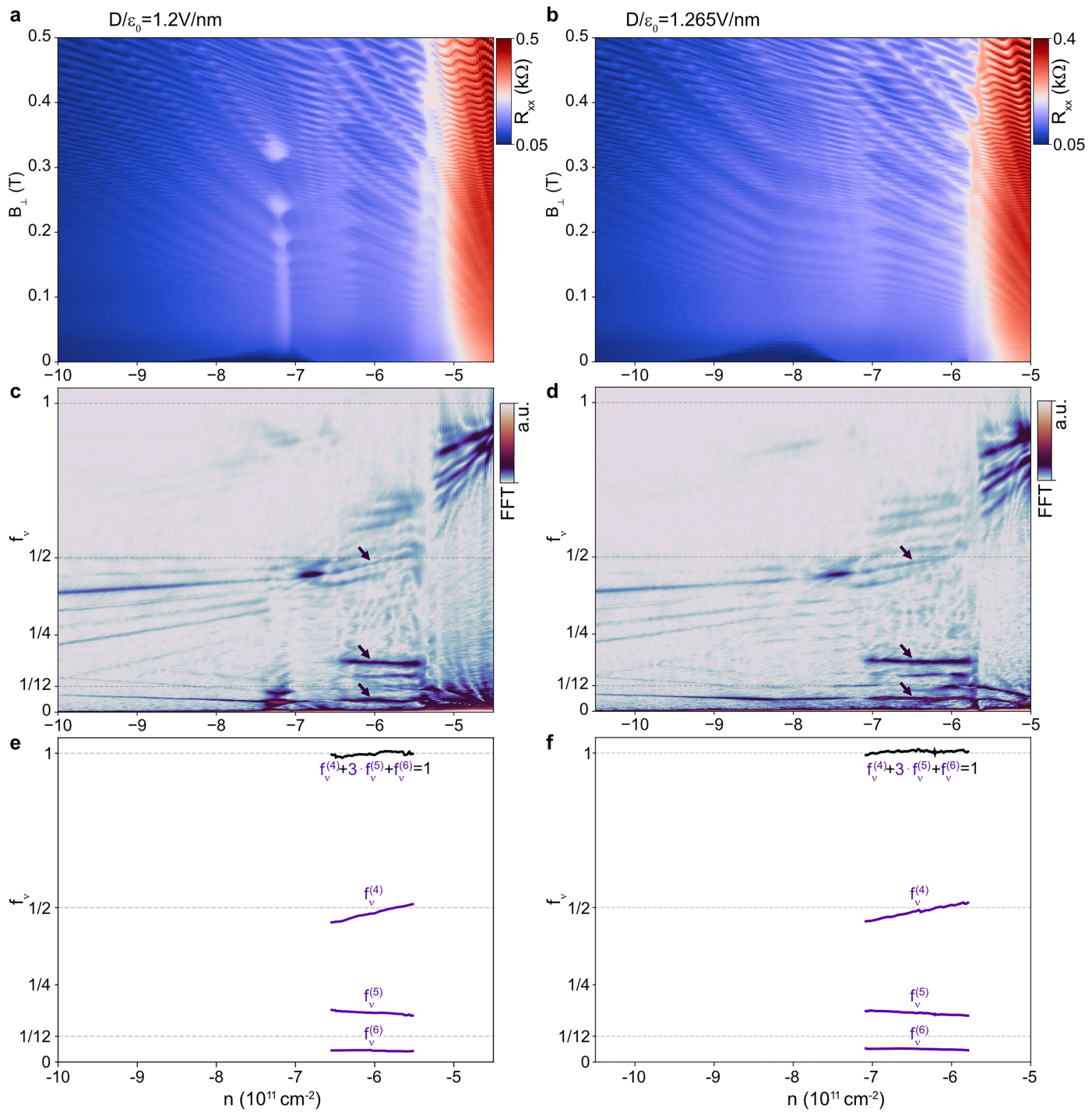
but plotted as a function of $1/B_\perp$. The corresponding frequencies are marked by colored arrows and lines. **c**, Intensity peaks in f_v extracted from the FFT data.



Extended Data Fig. 8 | FP(1, 3) and FP(1, 3, 1) at $D/\epsilon_0 = 0.85 \text{ V/nm}$ and 1 V/nm , respectively. **a, b**, R_{xx} versus out-of-plane magnetic field B_\perp and doping density n measured at $D/\epsilon_0 = 0.85 \text{ V/nm}$ (**a**) and 1 V/nm (**b**), respectively.

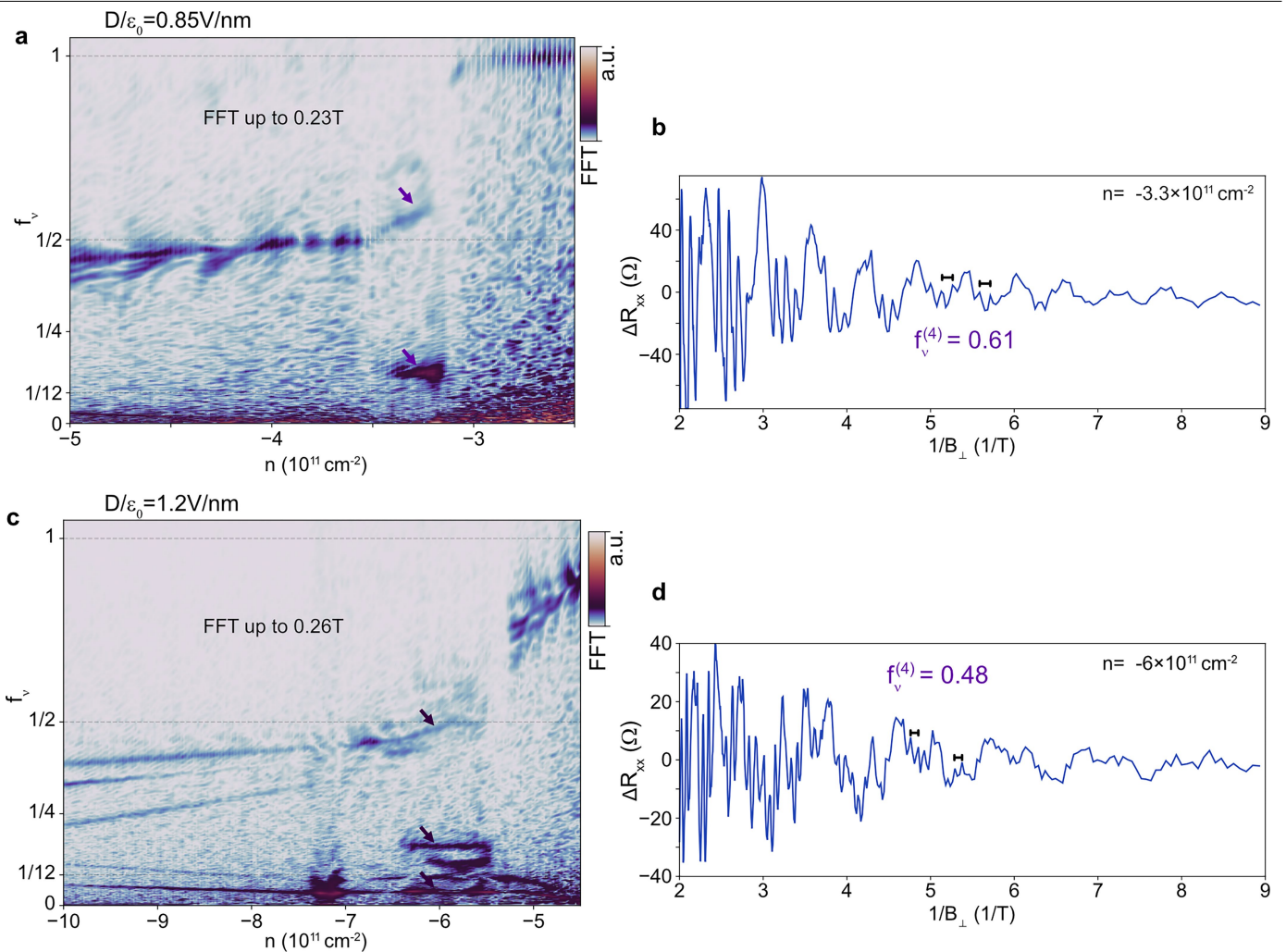
c, d, Frequency-normalized Fourier transform of $R_{xx}(1/B_\perp)$ (using data within $0.05 < B_\perp < 0.45 \text{ T}$) at $D/\epsilon_0 = 0.85 \text{ V/nm}$ (**c**) and 1 V/nm (**d**), respectively. **e, f**, Intensity peaks in f_v extracted from the FFT data in **c** and **d**.

Article



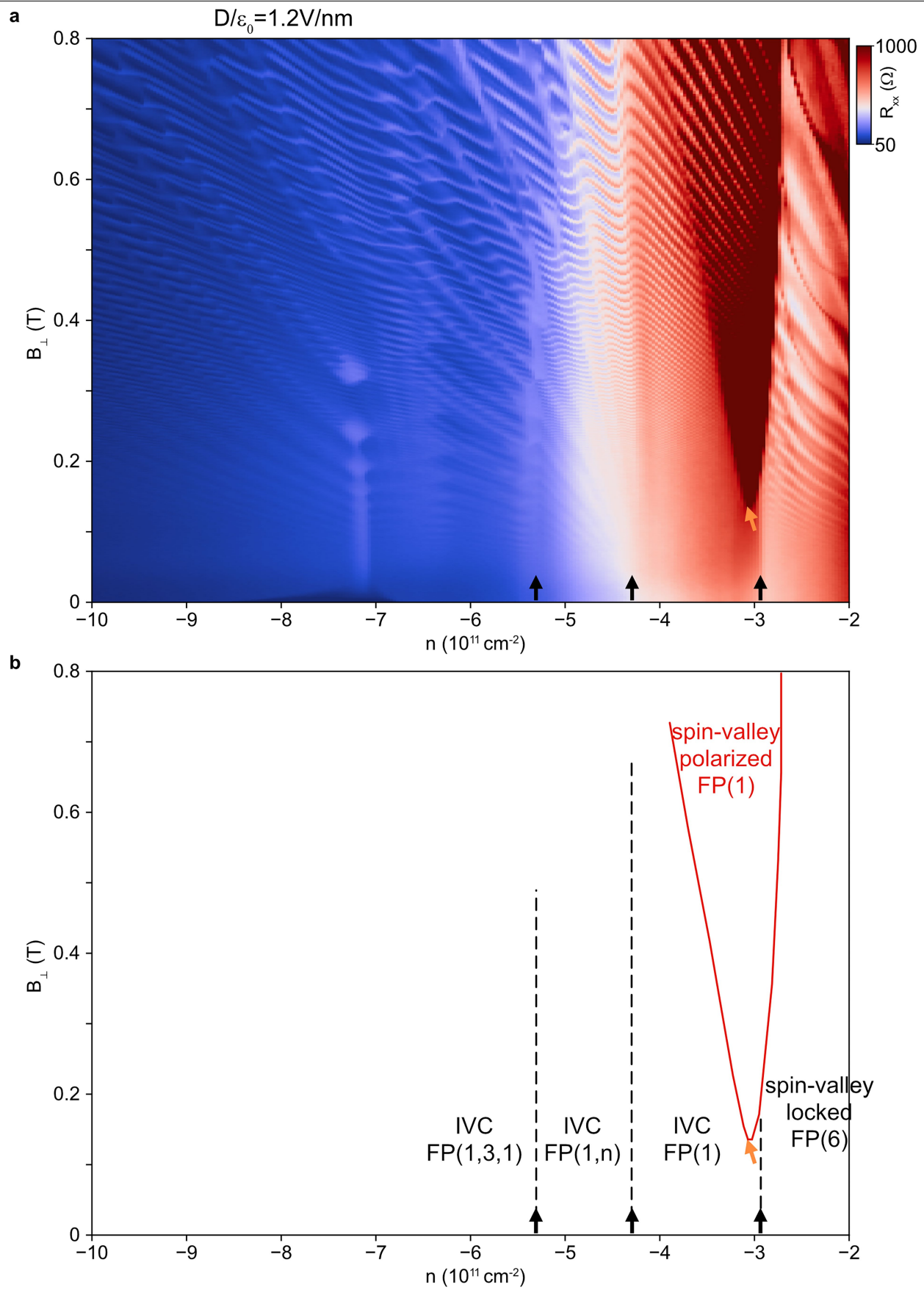
Extended Data Fig. 9 | FP(1, 3, 1) at $D/\epsilon_0 = 1.2 \text{ V/nm}$ and 1.265 V/nm . **a, b,** R_{xx} versus out-of-plane magnetic field B_\perp and doping density n measured at $D/\epsilon_0 = 1.2 \text{ V/nm}$ (a) and 1.265 V/nm (b), respectively. **c, d,** Frequency-normalized

Fourier transform of $R_{xx}(1/B_\perp)$ (using data within $0.05 < B_\perp < 0.45 \text{ T}$) at $D/\epsilon_0 = 1.2 \text{ V/nm}$ (c) and 1.265 V/nm (d), respectively. **e, f,** Intensity peaks in f_v extracted from the FFT data in c and d.



Extended Data Fig. 10 | FFT of FP(1, 3) and FP(1, 3, 1) with data at lower magnetic field. **a,c**, Frequency-normalized Fourier transform of $R_{xx}(1/B_\perp)$ at $D/\epsilon_0 = 0.85 \text{ V/nm}$ (**a**) and 1.2 V/nm (**c**), respectively. The R_{xx} data are used up to

0.23 T and 0.26 T respectively. **b,d**, R_{xx} variation ΔR_{xx} as a function $1/B_\perp$ measured at $n = -3.3 \times 10^{11} \text{ cm}^{-2}$, $D/\epsilon_0 = 0.85 \text{ V/nm}$ (**b**) and $n = -6 \times 10^{11} \text{ cm}^{-2}$, $D/\epsilon_0 = 1.2 \text{ V/nm}$ (**d**), respectively.



Extended Data Fig. 11 | See next page for caption.

Extended Data Fig. 11 | Evolution of phase boundaries as a function of B_{\perp} .
a, R_{xx} versus out-of-plane magnetic field B_{\perp} and doping density n measured at $D/\epsilon_0 = 1.2 \text{ V/nm}$ for a device with $|\lambda_i| \approx 1.5 \text{ meV}$. Phase boundaries are marked out in **b**. The black arrows and dashed lines mark the phase boundaries that are not

sensitive to B_{\perp} , suggestive of inter-valley coherence with little or no net orbital moments. The red line draws the phase boundary of the spin-valley polarized FP(1); the boundary grows (orange arrow) with B_{\perp} due to large orbital moments.